



Scale-free vertical tracking microscopy

Deepak Krishnamurthy ^{1,2}, Hongquan Li ^{2,3}, François Benoit du Rey², Pierre Cambournac², Adam G. Larson², Ethan Li ² and Manu Prakash ²

The behavior and microscale processes associated with freely suspended organisms, along with sinking particles underlie key ecological processes in the ocean. Mechanistically studying such multiscale processes in the laboratory presents a considerable challenge for microscopy: how to measure single cells at microscale resolution, while allowing them to freely move hundreds of meters in the vertical direction? Here we present a solution in the form of a scale-free, vertical tracking microscope, based on a 'hydrodynamic treadmill' with no bounds for motion along the axis of gravity. Using this method to bridge spatial scales, we assembled a multiscale behavioral dataset of nonadherent planktonic cells and organisms. Furthermore, we demonstrate a 'virtual-reality system for single cells', wherein cell behavior directly controls its ambient environmental parameters, enabling quantitative behavioral assays. Our method and results exemplify a new paradigm of multiscale measurement, wherein one can observe and probe macroscale and ecologically relevant phenomena at microscale resolution. Beyond the marine context, we foresee that our method will allow biological measurements of cells and organisms in a suspended state by freeing them from the confines of the coverslip.

espite being only a few hundredths of the biomass of terrestrial ecosystems¹, the oceans are responsible for half of the carbon fixed on our planet². Remarkably, this primary production in the ocean comes mostly from minuscule phytoplankton³, the majority of which are invisible to the naked eye. Key processes in the ocean, such as the biological pump of carbon^{3,4} that directly impact planetary scale biogeochemical cycles and atmospheric carbon levels, arise from the interactions of individual behaviors of microscale plankton and the sinking dynamics of small particles with stratified environments over vast vertical depths⁵. Therefore, understanding the biophysical mechanisms behind these processes inherently requires bridging vastly separated length (from microns to kilometers) and timescales (from milliseconds to days).

Tracking individual microscopic organisms or objects freely moving over macroscopic ecological scales of hundreds of meters is a fundamental experimental challenge. This is particularly highlighted in microscopy, where there is an inherent tradeoff between optical resolution and field of view (FOV)6. Conventional microscopes are typically designed to image in the horizontal plane, with small chamber heights of only a few millimeters⁷. This becomes a limiting factor in the study of objects with ballistic motility, which rapidly move across a fixed FOV. For organisms with dominant vertical movements, confinement results in strong boundary interactions and truncated track lengths, leading to a statistical bias, as objects with small diffusivities have a greater contribution to the short tracks⁶. Tracking microscopy offers a possible solution to this issue, where the object is kept within the optical FOV using various closed-loop tracking methods8-12 or for sinking particles using hydrodynamic levitation using a constant upward flow¹³. However, these approaches are not suitable for objects with active behavior or limit the object's movement to the maximum size of the chamber, which is ~100 mm (ref. 11) leading to a track length that is much smaller than ecological scales of interest (>10 m).

An ideal vertical tracking microscope that captures cellular details and allows unrestricted movement over ecological scales (greater than tens of meters) would require a meter to kilometer-long translational axis (Fig. 1a) and is not feasible due to

cost, space and practical constraints in translating delicate optical equipment over large distances. To overcome this challenge, here we present a 'hydrodynamic treadmill for single cells', which allows us to physically implement an autonomous vertical tracking microscope. The design consists of a vertically oriented, circular fluidic chamber with a horizontal rotation axis. A modular optical microscope is used to image the object under study with the FOV at either the 3 o'clock or 9 o'clock angular positions, such that rotating the chamber can appropriately compensate for a net vertical motion of the object. The instrument effectively provides unlimited scope for vertical motion (scale-free), while concurrently providing micronand millisecond-scale spatiotemporal resolution.

Doculto

Scale-free vertical tracking microscopy using a 'hydrodynamic treadmill'. The key components of the scale-free vertical tracking microscope are a circular fluidic chamber with a rotational axis and a horizontally positioned microscope with two-axis tracking (Fig. 1). The circular fluidic chamber plays a key role in preventing any tracked object from encountering boundaries in the vertical direction (z) (Fig. 1b,c). The fluidic chamber consists of an annular fluidic volume with inner and outer radii R_i and R_o and width W_i , so that the local cross-section is rectangular with dimensions $L \times W$, where $L = R_0 - R_1$ (Supplementary Fig. 1). Typical values used in experiments are $R_i = 85$ mm, L = 15, 30 mm and W = 3.2-6 mm. The fluidic chamber is attached to a fine rotational stage with a horizontal rotational axis (Fig. 1d and Extended Data Fig. 1), so that the chamber can be rotated with a fine angular incremental resolution (Methods). Tracking in the horizontal plane (xy) is achieved by translating the rotational stage using motorized linear stages with the optical assembly fixed in the laboratory frame or vice versa (Fig. 1d and Extended Data Fig. 1).

We mounted a custom-built light microscope focused on either the 3 o' clock or 9 o'clock position of the circular chamber (see Fig. 1b,c and Extended Data Fig. 1) such that rotational motion of the chamber results in tangential motion parallel to the axis of gravity at the center of the optical FOV (Fig. 1c and Supplementary Video 1).

¹Department of Mechanical Engineering, Stanford University, Stanford, CA, USA. ²Department of Bioengineering, Stanford University, Stanford, CA, USA. ³Department of Electrical Engineering, Stanford University, Stanford, CA, USA. [™]e-mail: manup@stanford.edu

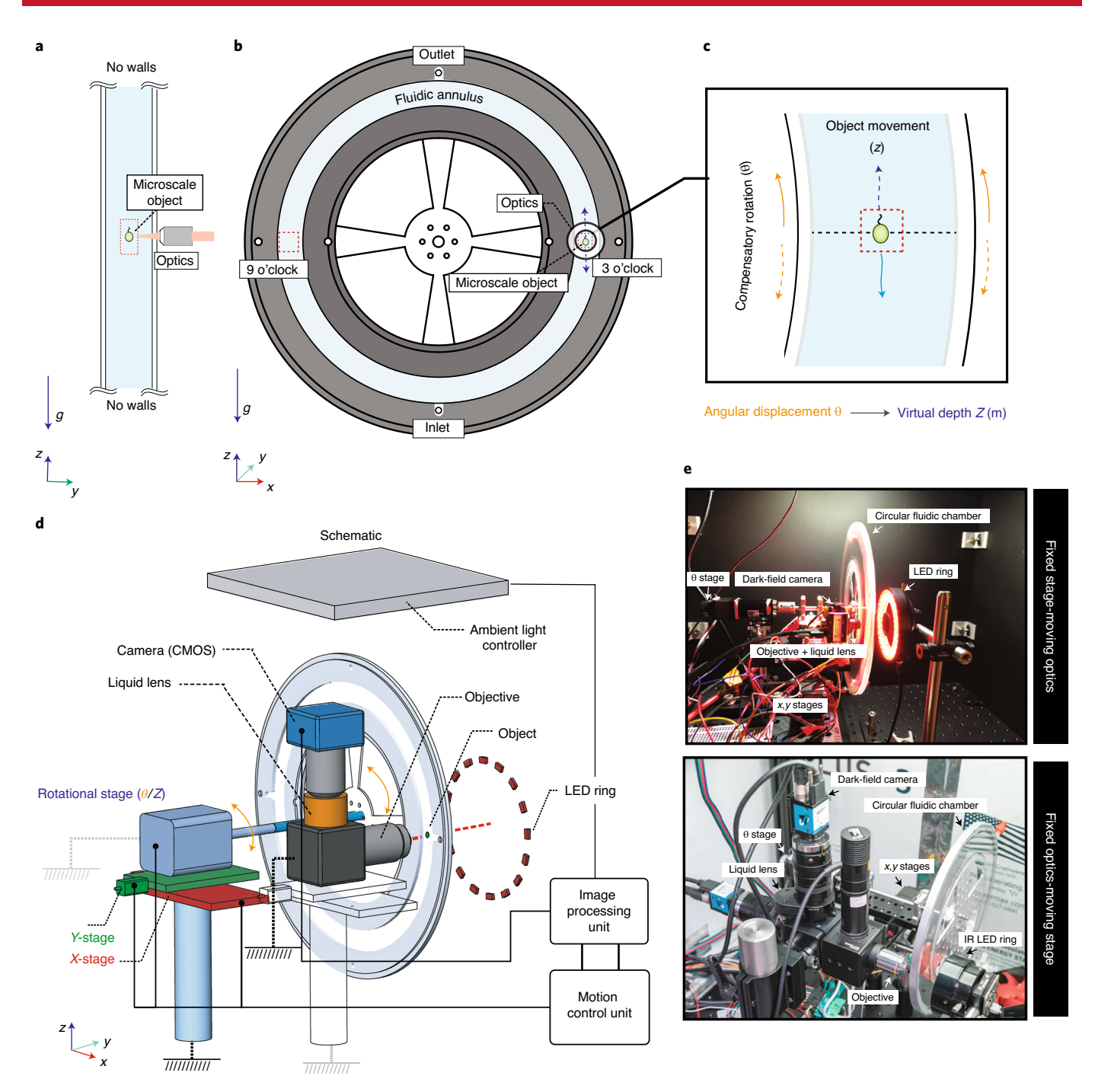


Fig. 1 | Scale-free vertical tracking microscopy using a hydrodynamic treadmill. a, Schematic of an ideal, scale-free vertical tracking microscope with no boundaries in the vertical direction. b, A vertically oriented circular fluidic chamber (henceforth, fluidic chamber), with a contiguous annulus of fluid as a realization of such a tracking microscope. c, A microscale object immersed in the ambient fluid is tracked at either of the 3 o'clock or 9 o'clock positions, wherein upward or downward movements of the object relative to the fluid are compensated by stage rotation in the opposite direction using a closed-loop tracking system. A 'virtual depth' for the object can be assigned from net angular displacement and radial position. d, Schematic of a practical implementation of the vertical tracking microscope (also see Supplementary Video 1 and Extended Data Fig. 1) showing the fluidic chamber and rotational stage for vertical (z) tracking, as well as translational stages coupled to the rotational stage such that the optical assembly is fixed in the laboratory frame. e, Photographs of the tracking microscope in the two configurations (also see Extended Data Fig. 1): (1) fixed-stage, moving optics and (2) fixed optics, moving stage. The latter is more suitable for implementing a wider range of optical systems. IR, infrared.

The microscope optics consist of a lens assembly constructed around a liquid lens with controllable optical power (Supplementary Figs. 2, 15 and 16). The liquid lens is used to rapidly modulate the focal plane of the microscope, which was used to achieve tracking along the optical axis (Methods; Supplementary Fig. 4). This assembly was

coupled to a CMOS camera capable of full-resolution color imaging at high sampling rates (238 Hz). The modularity of the optical system allows flexibility in switching between different imaging strategies (Extended Data Fig. 1a). In our experiments, we primarily used dark-field imaging using a ring light-emitting diode (LED) situated

on the side opposite to the imaging assembly (Fig. 1c and Extended Data Fig. 1). On the basis of the organism being tracked, we used a suitable wavelength of dark-field illumination, such that the organism's behavior was not perturbed (Supplementary Fig. 17)^{14,15}.

Images captured on the camera sensor were fed to a custom image-processing pipeline implemented on a computer and the object position was extracted rapidly (≈5 ms) using real-time machine vision algorithms (Methods; Supplementary Fig. 3). The resulting tracking error, which is defined as the displacement between the object position and center of the microscope's FOV (and focal plane), was relayed to a microcontroller, which in turn sent motion commands to the rotational and translational stages to track the object (Fig. 1d and Supplementary Fig. 2). The entire experimental setup was housed within a temperature- and light-controlled enclosure (Fig. 1e). An isothermalization procedure was implemented such that background flows in the chamber are <20 μm s⁻¹ (Methods; Supplementary Fig. 5). Ambient light intensities can be modulated as a function of 'virtual depth' of the tracked object using a top-mounted white LED array that provides uniform illumination across the experimental chamber (Fig. 1d,e and Extended Data Fig. 1).

A formalism for vertical tracking using a 'hydrodynamic treadmill'. Previously, vertical rotating viscous flows have been used to study the dynamics of immersed light or heavy objects 16-18, as well as for cell-culture applications in rotating-wall vessels to simulate microgravity 19,20. However, to our knowledge such a geometry has never been used as the basis of a vertical tracking microscope and as such, its physical feasibility, fundamental limits and design space are unknown. During tracking, small angular motions are imparted to the circular fluidic chamber to compensate for vertical motions of the tracked object. This has two effects: (1) imparting rotational momentum to a contiguous annulus of fluid via the circular fluidic chamber suffers a viscous delay leading to a transient flow profile that is not uniform (Extended Data Figs. 2 and 3a); and (2) tracking linear vertical motions using circular motion compensation is likely to have consequences for the measured track.

Motivated by these unique considerations, we carried out a detailed physical analysis to identify the parameter tradeoffs and to establish the design space of our vertical tracking method, in relation to the tracked object's properties. In contrast, considerations for horizontal tracking are similar to conventional Lagrangian tracking strategies in a fluid^{8–10,12} and are not discussed here. We confirmed that for parameters relevant to marine microscale plankton and particles (sizes $d \leq O(\text{mm})$, vertical speeds $u_{\text{obj}} < O(\text{mm s}^{-1})$ and density differentials $(\rho_{\text{obj}} - \rho_{\text{f}})/\rho_{\text{f}} \approx 10\%$, where ρ_{obj} and ρ_{f} are the object and fluid densities²¹), the system dynamics are linear and viscous effects dominate both the object's and fluid's inertia (Supplementary Discussion 2.2). We now detail three additional physical considerations to ensure tracking success and fidelity.

In general, any tracked object has a 'behavioral timescale' $\tau_{\rm obj}$ over which its vertical velocity changes (which scales as $\tau_{obj} = u_{obj}/a_{obj}$, where a_{obj} is the rate of velocity change about a steady-state velocity $u_{
m obj}$). This timescale can be either slow $(au_{
m obj}\gg au_{
m tracking})$ or fast $(au_{
m obj} \ll au_{
m tracking})$ compared to the dynamics of the tracking system, typically corresponding to abiotic (such as a sinking microsphere) and biotic objects (such as a swimming plankton cell), respectively. To understand tracking performance in both these limits we carried out a detailed analysis of the stage and fluid dynamics (Supplementary Discussion 2.3 and Extended Data Fig. 2) during a tracking move that compensates for a change in an object's vertical velocity. Our analysis results in a succinct mathematical condition that allows one to estimate the tracking success based on four timescales, two involving the object being tracked and two others involving the tracking system parameters (Supplementary Discussion 2.3 and Extended Data Fig. 2). This is given by: $\tau_{\text{stage}} + \tau_{\text{visc}} < \tau_{\text{obj}} + \tau_{\text{FOV}}$

where $\tau_{\rm stage}$ is the mechanical response time of the stage and $\tau_{\rm FOV}$ is the time needed for the object to swim the optical FOV (of size $L_{\rm FOV}$ given by $\tau_{\rm FOV} = L_{\rm FOV}/u_{\rm obj}$). Here $\tau_{\rm visc} < W^2/4\nu$ is the viscous delay for momentum transfer to the fluid due to the contiguous circular fluidic chamber²².

This viscous delay also means that the flow in the chamber is transiently nonuniform during a change in rotation rate of the chamber (Extended Data Fig. 3a). By solving for the fluid's motion during a change in stage rotation rate, we derived both the magnitude of stress as well as rotational torque on a small organism due to this transient shear (Supplementary Fig. 8) and confirmed that there is a broad range of parameters (for instance in choosing the rotational acceleration of the stage), where the effects of this shear are negligible compared to the organism's intrinsic orientation fluctuations and aligning gravitactic torques (Extended Data Fig. 3a,b). Apart from the above effects on object orientation, weak shear can also affect measured trajectories due to phenomena such as bacterial rheotaxis²³, shear-induced trapping²⁴ as well as oscillatory rheotaxis near surfaces²⁵. However, each of these effects are only important beyond shear rates of 1 s-1 and are therefore likely subdominant in our current implementation because 1 s⁻¹ is the maximum transient shear rate based on chosen parameters (Supplementary Fig. 8). However, this factor needs to be considered when designing the annular geometry and associated stage-motion parameters for experiments.

Last, we find that tracking linear vertical motions using a circular motion compensation leads to a small radial drift that is given by $u_{\rm drift}/u_{\rm obj} = \Delta z/R(t)$, where Δz is the vertical tracking error and R(t) is the object's instantaneous radial position (Extended Data Fig. 3c). Note that this drift arises purely from a geometrical effect and is not due to a radial pressure gradient, which is negligible (Supplementary Discussion 2.2). This drift velocity is small compared to the organism's intrinsic horizontal velocities (Extended Data Fig. 3d) and for most table-top setups, with R_i and R_o in the O(10)cm, this radial drift is negligible when the tracking error is within a microscope FOV. For long-term tracking, this error can be calculated and compensated for.

Overall, our analysis reveals that a large region of parameter space exists in which biotic and abiotic microscale objects can be tracked successfully in practice, with the measured tracks not differing significantly from tracks that would be measured in a quiescent fluid. Our analysis also provides a crucial design tool to optimally set up the parameters of the tracking system given some known properties of a microscale plankton or abiotic object of interest. Next, we validated our method by measuring the sedimentation speed of 250-µm density calibrated beads and comparing the results to those measured using conventional Eulerian tracking in a vertical cuvette (15-cm tall and with the same cross-section as the fluidic chamber) (Supplementary Fig. 6). The two sedimentation speeds exhibited good agreement among six different types of beads measured and the measured speeds also agreed with the theoretical Stokes law predictions (Supplementary Fig. 6). Having characterized and validated our tracking method, we now use it to report multiscale measurements of plankton behaviors over eight major marine phyla. Simultaneously, these measurements push the boundaries of both the smallest and largest spatiotemporal scales for these measurements by bridging length scales of microns to meters and timescales of milliseconds to hours, in the process revealing new phenomena across scales.

Free-swimming behavior and microscale flow fields of invertebrate larvae. Most marine invertebrate larvae have a microscale planktonic phase with complex morphology and behavior. These behaviors, which include swimming, feeding and ultimate settlement responses are crucial in understanding the biogeography of benthic ecosystems^{5,26}. Despite the importance of this problem, it

has been challenging to study due to its multiscale nature. Using a diversity of species with equally diverse swimming strategies, we now demonstrate long-distance tracking of free-swimming invertebrate larvae. In addition to the macroscale three-dimensional (3D) track, we concurrently measure larval shape, posture, orientation, specific feeding and swimming behavior and hydrodynamic flow fields. Here we present data for eight species of marine benthic invertebrates, all indigenous to the coast of Northern California, USA (Supplementary Table 1). The larvae spanned four phyla and five classes across the animal kingdom (Fig. 2).

We measured 3D tracks of individual larvae swimming over timescales of several hours and vertical extents of a few meters. Figure 2 shows a representative subsample of the eight larvae species over a 5-min interval exhibiting a diversity of swimming behaviors across scales (Supplementary Video 2). Notably, all larvae exhibit vertically biased motility evident in the anisotropic distributions of vertical and horizontal velocities (Fig. 2(iv) and Supplementary Fig. 7)3,27. We confirmed that this vertical bias was due to intrinsic behavior and not caused due to the chamber walls (Supplementary Discussion 2.5 and Supplementary Figs. 12 and 13). The most striking example of this vertically biased motility was in polychaete larvae (Owenia sp.; Fig. 2a(iii,iv)), which swam downward for a distance of 364 mm (182 microscope FOVs) over 5 min while having a negligible horizontal excursion (Supplementary Fig. 7). At the largest scales, the vertical motility of larvae was split between active upward or downward swimming, where the anterior-posterior axis of the larvae was parallel or antiparallel, respectively, to gravity; and passive/active sinking, where the larvae had an upward orientation but downward vertical velocity (Fig. 2(iii) and Supplementary Video 2). The multiscale nature of the measurements revealed characteristic behaviors even at an order-of-magnitude smaller scale, as seen from the mesoscale tracks plotted over a vertical extent of 5 mm (Fig. 2(ii)). Behavior at the mesoscale was characterized by swimming motifs including helical swimming (Fig. 2a,d,f,h(ii)), free-fall (Fig. 2b,c(ii)), hovering (Fig. 2b,c,h(ii)) and pauses and reversals due to changes in ciliary beat (Fig. 2c,g(ii) and Supplementary Video 2).

Together with tracking, we observed the microscale behavior, posture and shape of the larvae from images acquired at millisecond time resolution (Fig. 2(i)). By seeding the fluid with tracer particles, we measured the dynamic flow fields around freely swimming larvae using particle image velocimetry (Fig. 2b,e,g,h insets; Supplementary Methods). These flows, shown in the laboratory reference frame by subtracting the translational velocity of the larvae, arise from the interplay of larval shape, density and fluid stresses generated by the ciliary band (Fig. 2: larvae sketches)^{26,28}. In particular, we observed characteristic flows when the larvae maintained their position in the water column and created a feeding current to scan the water for food particles (Fig. 2b,h insets). For the larvae of Schizocardium californicum, we observed a striking dipolar velocity field due to the wide separation between the ciliary band responsible for propulsion (circular skirt at the posterior end of the larvae) and the rest of the larval body, which has no propulsive

contribution (Fig. 2e inset)²⁹. In all larvae, subtracting the translational component of the velocity field revealed a strong Stokeslet contribution¹¹, which occurs because these larvae have an excess density to sea water and thus need to create propulsive stresses just to maintain their position in the water column (Fig. 2g inset).

Tracking motile single cells. Going down one order in length scale, we next tracked planktonic protists. Protists are a ubiquitous and diverse category of unicellular eukaryotic microorganisms and they lie at the base of the entire marine food web³⁰. These organisms display a diversity of body sizes, cell forms and motility strategies. Motile species include planktonic uniflagellates, dinoflagellates and ciliates, which can actively swim in the water column. Population-scale measurements indicate that many dinoflagellates undergo diel migrations over scales of tens of meters³¹ but observing these organisms at subcellular scales to connect their behavior to cell biological processes has been a challenge. As a demonstration of our tracking method, we performed multiscale tracking of two marine species and two freshwater species of protists.

We successfully tracked marine dinoflagellates, including Akashiwo sanguinea and Ceratium sp. collected from Monterey Bay, California, which are often responsible for red tides in that region. For A. sanguinea, we observed two distinct cell states undergoing positive and negative gravitactic behaviors, respectively, under the same environmental conditions. The cell orientation was different for each population, such that the cells actively swam down and up for the positive and negative gravitactic behaviors, respectively (Supplementary Movie 3). In contrast for Ceratium sp., we observed only positive gravitaxis. For both species, motility was biased along the axis of gravity (for example for A. sanguinea, mean ± s.d. in vertical and horizontal velocities was $V_z = 274 \pm 284 \,\mu\text{m}\,\text{s}^{-1}$ and $V_r = 11 \pm 175 \,\mu\text{m s}^{-1}$, respectively and for Ceratium sp. this was $V_z = 127 \pm 172 \,\mu{\rm m \, s^{-1}}$ and $V_x = 11 \pm 89 \,\mu{\rm m \, s^{-1}}$, respectively) and the distributions in vertical and horizontal velocities for both species were significantly different (Kolmogorov–Smirnov test, P < 0.001).

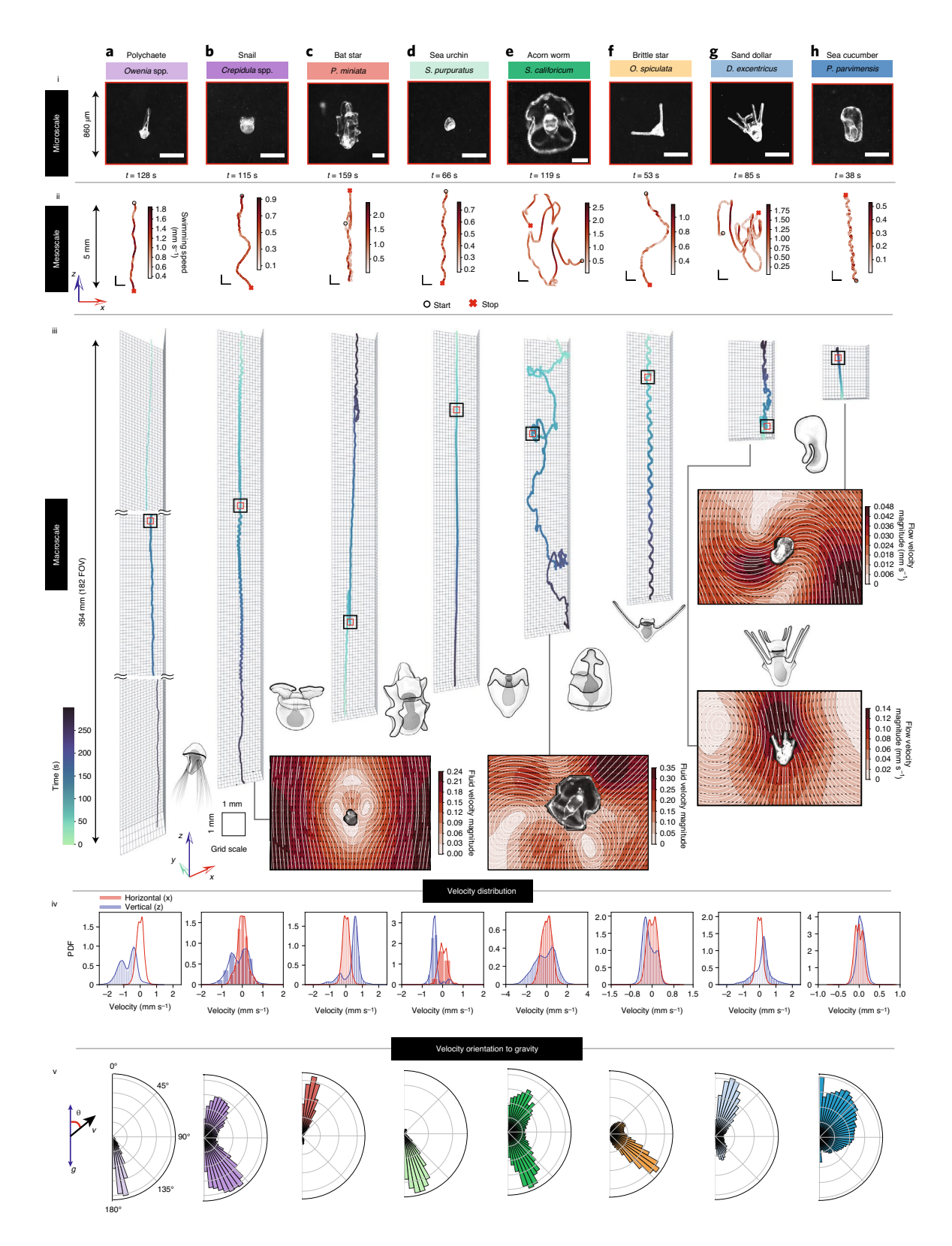
To compare and contrast these findings with freshwater organisms, we next studied two freshwater protists: the ciliate *Stentor coeruleus* and the alga *Euglena gracilis*. For *E. gracilis*, we found a positive gravitactic behavior as reported by others³². In *S. coeruleus*, we discovered a positive gravitactic behavior, where the cell swam with a downward orientation (anterior–posterior axis aligned with gravity) but with several ciliary reversals causing it to have a large range of vertical velocities (Fig. 3c(ii) and Supplementary Video 3). While photo responses of *S. coeruleus* have been studied³³, we report here its behavior under the effects of gravity alone, which raises the question of possible gravitaxis mechanisms.

Multiscale imaging of plankton behavior reveals microscale behavior repertoires. We now focus on *Patiria miniata* (bat star) larvae to further demonstrate how long-term tracking can reveal multiscale behavioral dynamics in a single plankton. We measured the free-swimming behavior of these larvae (ten larvae, total track

Fig. 2 | Multiscale measurements of free-swimming behavior and flow fields of invertebrate larvae. a-h, Columns represent different species of larvae: Owenia sp. (polychaete worm) (a), Crepidula sp. (snail) (b), P. miniata (bat star) (c), S. purpuratus (purple sea urchin) (d), S. californicum (acorn worm) (e), Ophiothrix spiculata (spiny brittle star) (f), D. excentricus (Pacific sand dollar) (g) and Parastichopus parvimensis (warty sea cucumber) (h). Rows (i-v) indicate concurrent measurements of larval behavior over different length and timescales. Upper to lower rows indicate increasing length and timescale. Row i, snapshots of freely swimming larvae from the tracks. Scale bars, 250 μm. Row ii, mesoscale xz projection of tracks shown over a vertical extent of 5 mm. Scale bars, 500 μm. Row iii, macroscale 3D tracks colored by elapsed track time. The red and black boxes correspond to the snapshots and mesoscale tracks shown in rows i and ii, respectively. The grid size is 1 mm ×1 mm. Row iv, distributions of vertical (z) and lateral (x) velocities for each larva, calculated over several tracks. PDF, probability density function. Row v, orientation distributions of the velocity vector relative to the vertical axis with 0° corresponding to upward swimming. Dual-lobed distributions in the cases of v, b and e correspond to organisms that exhibited upward and downward swimming phases even within the same trajectory. Rows iii-v highlight anisotropic, vertically biased motility. Additionally, flow fields around freely swimming larvae can be simultaneously measured using particle image velocimetry. These velocity fields are shown in the laboratory frame of reference for b,e,g,h.

duration $\approx 1.5\,\text{h}$) and found a vertically biased motility, where the larvae swam upward in a helical path (Fig. 4a) with an associated rotation of the larva body (Supplementary Video 4). We observed that the upward swimming was punctuated by a rapid behavioral transition (henceforth referred to as 'blink') from an upward to downward movement (Fig. 4b). Previously, these blinks have been discussed in the context of neuronal control of ciliary bands in

tethered larvae³⁴. Using long timescale tracks, we report the distribution and repeatability of this blinking behavior in free-swimming larvae. At the macroscale, blinks cause the larvae to sink for brief periods, thereby affecting their depth in the water column (Fig. 4b, *z*-track). Upon microscale interrogation of the blinks, we found that the blinks consisted of two behavioral microstates: a period of passive sinking, followed by a period of hovering or slower sinking.



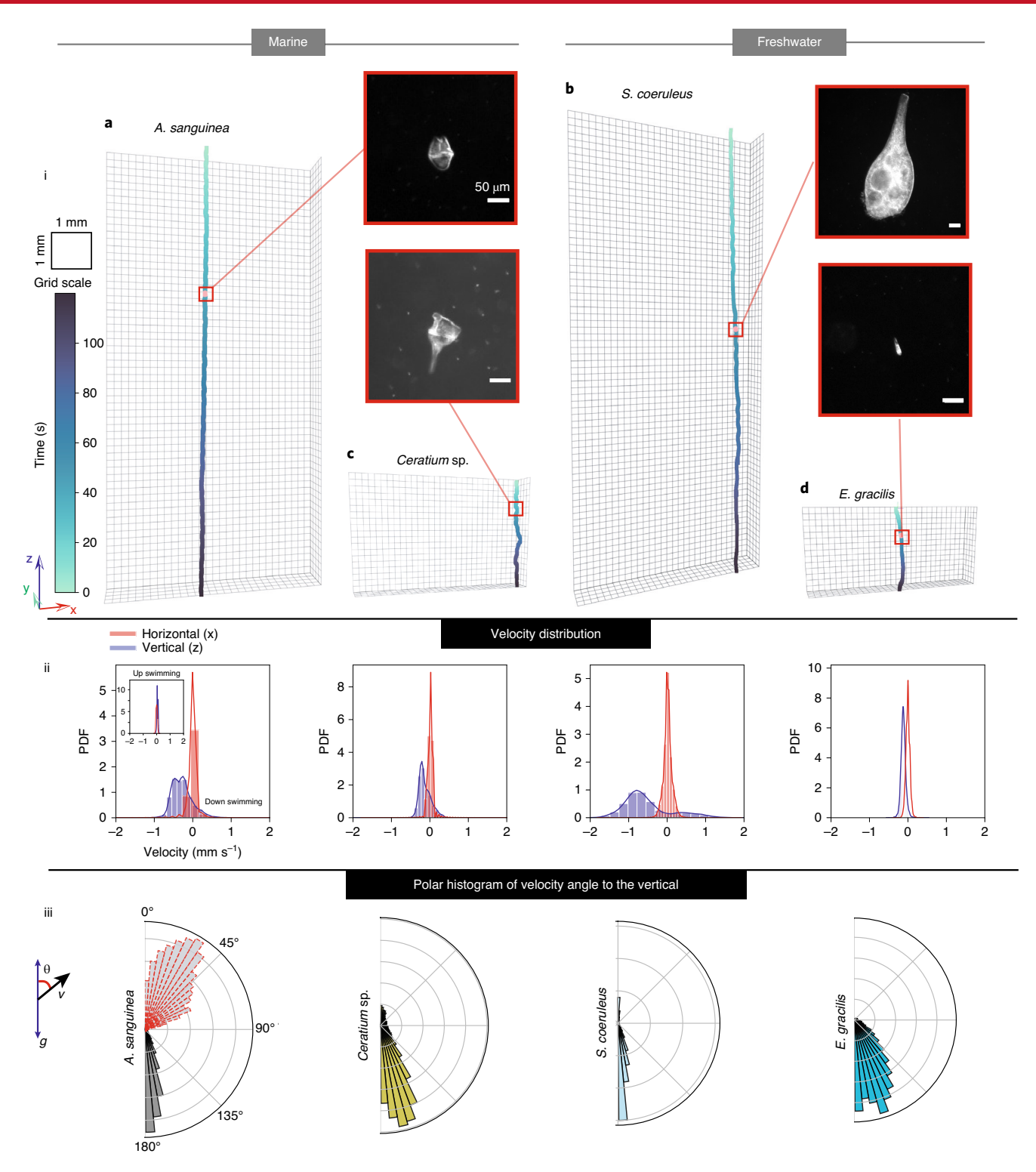


Fig. 3 | Tracking single-celled protists. a-d, We tracked two ecologically relevant marine dinoflagellates, *A. sanguinea* (**a**) and *Ceratium* sp. (**b**), as well as two freshwater motile cells, namely a large ciliate, *S. coeruleus* (**c**) and *E. gracilis* (**d**). Row i, representative 3D trajectories over a time interval of 2 min reveal vertically biased trajectories for all species (*A. sanguinea* n = 7 organisms, *Ceratium* sp. n = 5, *E. gracilis* n = 7 and *S. coeruleus* n = 5). Boxed insets correspond to video microscopy images obtained simultaneously at a subcellular resolution. Scale bars, 50 μm. Row ii, velocity distributions of vertical (*Z*) and horizontal (*X*) velocities for all organisms are anisotropic and vertically biased (mean ± s.d. in velocities $Vx = 1 \pm 176 \, \mu \text{m s}^{-1}$, $Vz = 274 \pm 284 \, \mu \text{m s}^{-1}$ for *A. sanguinea* and $Vx = 16 \pm 114 \, \mu \text{m s}^{-1}$, $Vz = 538 \pm 625 \, \mu \text{m s}^{-1}$ for *S. coeruleus*). Row iii, polar histogram of the angle of the velocity vector relative to the vertical axis of gravity. The distribution of *θ* highlights the anisotropic and positive gravitactic behavior of these cells.

We also found that dynamic changes in the flow field around the larva accompanied these behavioral changes. During upward swimming we measured a streaming flow past the larva (Fig. 4f(i)), while

during the hovering/slow-sinking phase we observed development of a striking array of up to four recirculating regions of flow attached to the larval body (Fig. 4f(ii-iv)). These flows, measured here in a

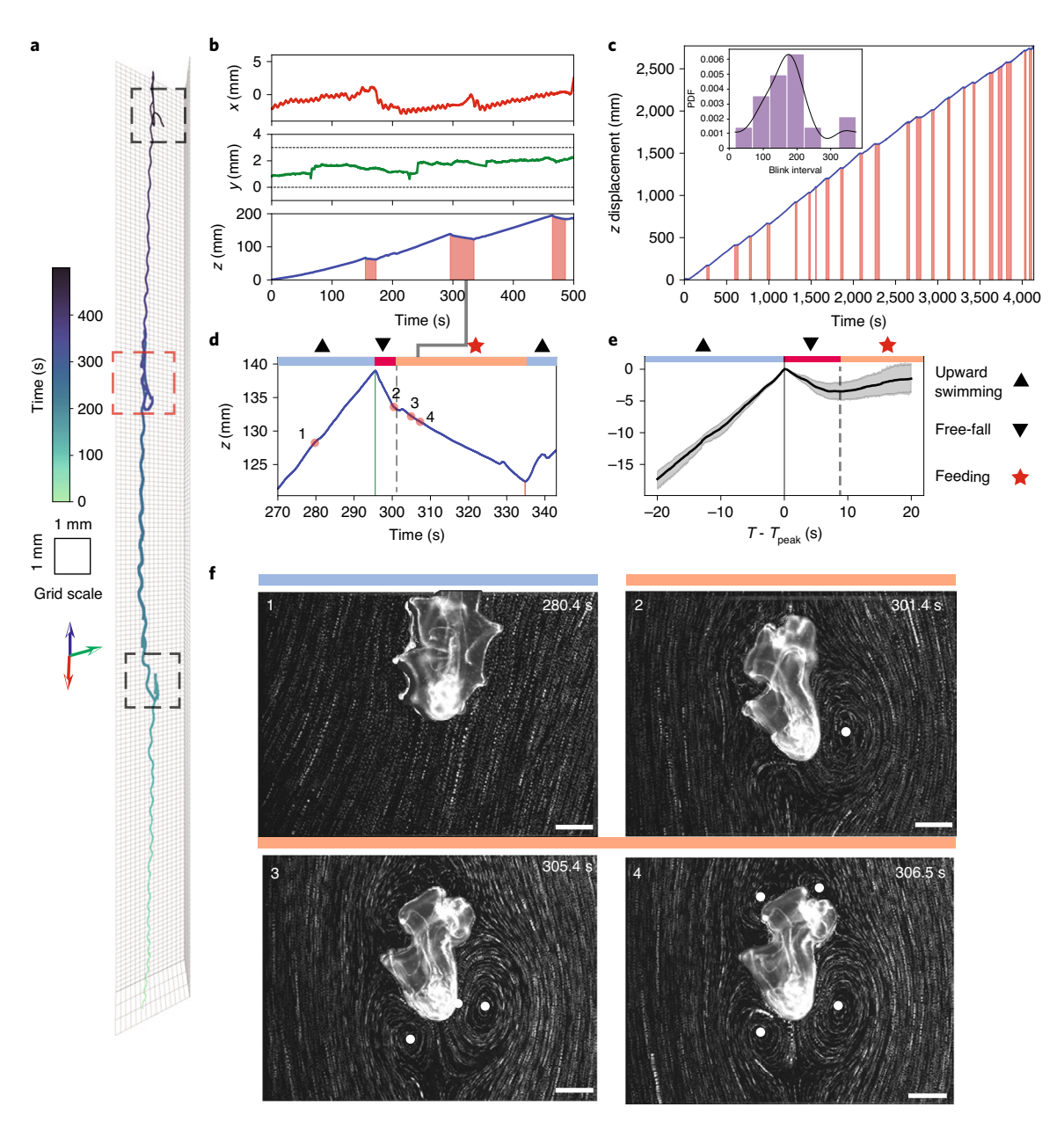


Fig. 4 | Multiscale behavioral measurements of *P. miniata* **larvae. a**, Representative 3D track showing the larva swimming upward in a columnar trajectory punctuated by three behavioral transitions (dashed boxes), called blinks (n=10 distinct organisms tracked, Supplementary Video 4). **b**, Position time traces reveal that these blinks involve a transition from upward swimming to periods of downward motion (red bands, bottom). **c**, Another track showing the vertical displacement of single larvae over a much longer timescale (>1h) with 23 behavioral transitions (red bands) while the larva swims up a distance of ≈2,500 mm (≈1,250 microscope FOV). Inset, the distribution of the intervals between blinks with mean±s.d. (175±78s). **d**, High spatiotemporal resolution tracking uncovers three distinct behavioral substates during each blink, consisting of a sequence of upward swimming (upward triangle), free-fall (downward triangle), feeding (star) and upward swimming. **e**, Behavior averaged by centering the tracks at the transition point from upward to downward displacement, over 23 blinks (mean, solid line and 95% CI, gray-filled region) shows the typical character of this behavioral sequence. **f**, Representative snapshot of fluid path lines around the larva during a blink show transitions in the flow field as a function of the behavioral substates (1–4). During upward swimming the flow has the signature open streamlines as seen in **f**(1), whereas in the feeding state the larva creates up to four recirculating regions (centers marked by white dots) adjacent to its body (Supplementary Video 4). Feeding also involves a characteristic change in larval body shape and a widening of the oral hood (**f**(2-4)). Scale bars, 250 μm. Behavioral transitions were observed across all ten tracking experiments.

co-moving reference frame^{35,36} by following untethered organisms using our tracking method, are part of the larva's feeding behavior and allow the larva to stay in a relatively fixed location in the water column, using gravity as a tether, while scanning a volume of water for food particles^{26,28}.

Our tracking method allowed us to follow individual larvae over long durations (Fig. 4c; track duration ≈4,000 s), enabling robust

measurement of the statistics of these behavioral transitions, which lasted $28\pm13\,\mathrm{s}$ and recurred with a time interval of $175\pm78\,\mathrm{s}$ (Fig. 4c, inset). Long time measurements also allowed us to extract the stereotypical behavior at the microscale during these transitions by aligning the vertical displacement tracks at the transition points from upward swimming to sinking (Fig. 4e). The behavior shows a universal profile where the sequence of microbehavioral states,

consisting of upward swimming, sinking and feeding, followed by upward swimming again, was conserved across a large number of blinks (Fig. 4e, n = 23). Our multiscale measurements highlight the dual function of blinks and the involvement of macroscale (depth regulation)³⁷ and microscale (feeding)^{26–28,38–40} components that are intimately linked.

Diel migration at the scale of individual plankton. An important macroscale consequence of plankton behavior is diel vertical migration, in which plankton rise toward the surface during the night and return to deeper waters during the day. How organisms regulate this diel behavior, and hence their positions in the water column as a function of different environmental cues, is an area of active research^{15,37,41}. Although the phenomenon is deeply linked to circadian rhythms over a 24-h cycle, previous experimental efforts have focused on the collective behavior of populations¹⁵ or have been technically limited in characterizing the behavior of single organisms or individual cells over long timescales. This has led to challenges in reconciling laboratory measurements of motility with the extent of vertical migrations observed in the field⁶.

We measured vertical migrating behaviors of polychaete larvae (Owenia sp.) during different times of the day, while maintaining other experimental conditions as constant. In particular, the larvae were imaged in red light (peak spectrum 620 nm; Supplementary Fig. 17) to which they are insensitive¹⁵, so as to not provide any light cues and furthermore in a medium with no food sources, such that the larvae were in a low-information environment. Tracks of different larvae (n=6, total track duration 616s) measured during davtime hours (between 13:00 and 15:00, local time) showed a markedly downward vertical swimming velocity ($v_z = -0.92 \pm 0.57 \,\mathrm{mm \, s^{-1}}$), while those measured at night (between 22:00 and 00:00, local time) swam upward ($v_z = 0.42 \pm 0.44 \,\mathrm{mm \, s^{-1}}$, n = 5, total track duration 360s (Fig. 5a,b, Kolmogorov-Smirnov distance between day and night vertical (z) velocity distributions: D=0.91, P<0.001, horizontal (x) velocity distributions: D=0.1, P<0.001). Notably, we found that the larvae actively reorient to swim upward or downward (Fig. 5a, inset; Supplementary Video 5). Such measurements of active upward and downward swimming have been reported for planktonic larvae at the scale of populations¹⁵, but not at the scale of individual organisms. The capability to observe long-distance diel migration of a freely swimming single organism and at microscale resolution, opens up the means to study how physiological states such as circadian rhythms⁴² interact with external cues to program this fascinating behavior.

Measuring behavior in virtual depth-patterned environments.

Organisms migrating in a stratified ocean encounter changes in physical parameters such as light. By mapping variations of ambient parameters to temporal variations and/or variations in the 'virtual depth' of the tracked organism, we can program arbitrary depth-patterned environments. This technique enables us to program both extremely sharp but also extremely shallow ecological-scale gradients. We demonstrate this environmental patterning using a light cue that is coupled to a virtual-depth parameter using an ambient light controller (Fig. 1d). For the purposes of demonstration, we chose an artificial, depth-based light-intensity pattern, such that every change in virtual depth of 20 mm triggered alternately a light-dark (L-D) or dark-light (D-L) transition in the ambient white illumination light intensity, resulting in a 'virtual reality arena, such that the organism's motions would directly control its ambient environment. As a test subject, we used the colonial alga Volvox, which is made up of hundreds of somatic ciliated cells and which has a well-documented phototactic response⁴³.

We tracked individual colonies of *Volvox aureus* as they navigated a depth-patterned light environment and triggered alternating D–L and L–D transitions as a function of virtual depth (Fig. 5c).

By tracking individual colonies over a long timescale, we were able to measure a number of these transitions (n = 25) as the colony swam upward by 1 m. Though not visible over the vast vertical scale of the track, the multiscale nature of our measurements revealed that the transition from D-L had a significant effect on the swimming behavior compared to swimming during no transitions, causing the colony to transition from upward swimming to a brief sinking period, which in turn caused a second series of L-D and D-L transitions as the colony sank below the depth-based threshold for the transition (Fig. 5c and Supplementary Video 6). In contrast, the L-D transition did not cause any significant change in swimming behavior, which was statistically indistinguishable from a period of no transition (Fig. 5c and Supplementary Video 6; Kolmogorov-Smirnov pair-wise comparison of velocity distribution in the neighborhood of a D-L and L-D transition, $D_{DL \text{ versus LD}} = 0.16$, P < 0.001; D-L versus no transition, $D_{\text{DL versus noTrans}} = 0.13$, P < 0.001; and L-D versus no transition, $D_{\rm LD\ versus\ noTrans} = 0.03$, P = 0.0001). This asymmetric response to D-L and L-D transitions was confirmed by measuring the mean behavior after aligning the vertical velocity traces of several transition events, which displayed universal profiles for D-L and L-D transitions (Fig. 5d,e). The measured mean behavior also confirmed that the brief sinking period triggered by the D-L transition was short-lived and that the colony resumed its upward swimming, which is consistent with a transient change in ciliary beat frequency and subsequent adaptive response of the cilia, as reported by others using different methods⁴³. The transition in the ciliary beat form had a second signature not reported previously, whereupon the natural rotation frequency of the colonies was perturbed: during a D-L transition the colony transiently rotated faster with $\omega_{\text{transition}} = 0.217 \pm 0.016 \,\text{s}^{-1}$ (n = 10 transitions) compared to the resting rotation rate during either constant light or dark conditions $\omega_{\text{resting}} = 0.125 \pm 0.014 \,\text{s}^{-1}$ (see Supplementary Video 6).

Comparative analysis of plankton behaviors across scales. Using scale-free vertical tracking microscopy, we have reported both the longest as well as finest spatiotemporal measurements to date of plankton behaviors across eight eukaryotic phyla. From comparison of trajectories across 14 species, a unifying theme of our measurements and our most significant finding, emerges: there are ubiquitous highly persistent gravitactic behaviors in both unicellular and multicellular plankton and these behaviors lead to vertical displacements that far outstrip horizontal displacements (Fig. 6a,b). Remarkably, in all but one of the species surveyed here, displacements along the vertical direction exhibit ballistic transport (slope of mean squared displacement (MSD) ~2) for even the longest measured trajectories (for instance $T_{\text{max}} \approx 4{,}100 \text{ s}$ for *P. miniata* larvae, $T_{\text{max}} \approx 700 \text{ s}$ for Strongylocentrotus purpuratus larvae; Supplementary Table 5). In contrast, the horizontal velocity decorrelates over timescales on the order of seconds for all species surveyed here (Supplementary Fig. 7 and Supplementary Table 5). This tight coupling of the velocity vector to the axis of gravity points to active and/or passive mechanisms for gravitaxis across unicellular and multicellular plankton. We have further confirmed that these vertically biased behaviors are due to intrinsic factors and are not due to confinement or other tracking effects (Supplementary Figs. 12 and 13). Compared across all species, the slope of vertical MSD reveals a cluster around the ballistic regime (MSD_z $\sim t^2$) (Fig. 6c) but with significant variability. The variability in a long time slope across different species, which is a key aspect of species-specific behavioral models for dispersal, can be quantitatively linked to microscale behaviors of the organisms, such as ciliary reversals, feeding events and other changes that affect vertical velocity. We find that this slope shows a negative correlation to the variability in vertical velocity (P = 0.001; Fig. 6c), with most surveyed plankton exhibiting ballistic and super-diffusive behaviors, and only S. californicum larvae exhibiting dispersal rates near the diffusive limit (slope \sim 1).

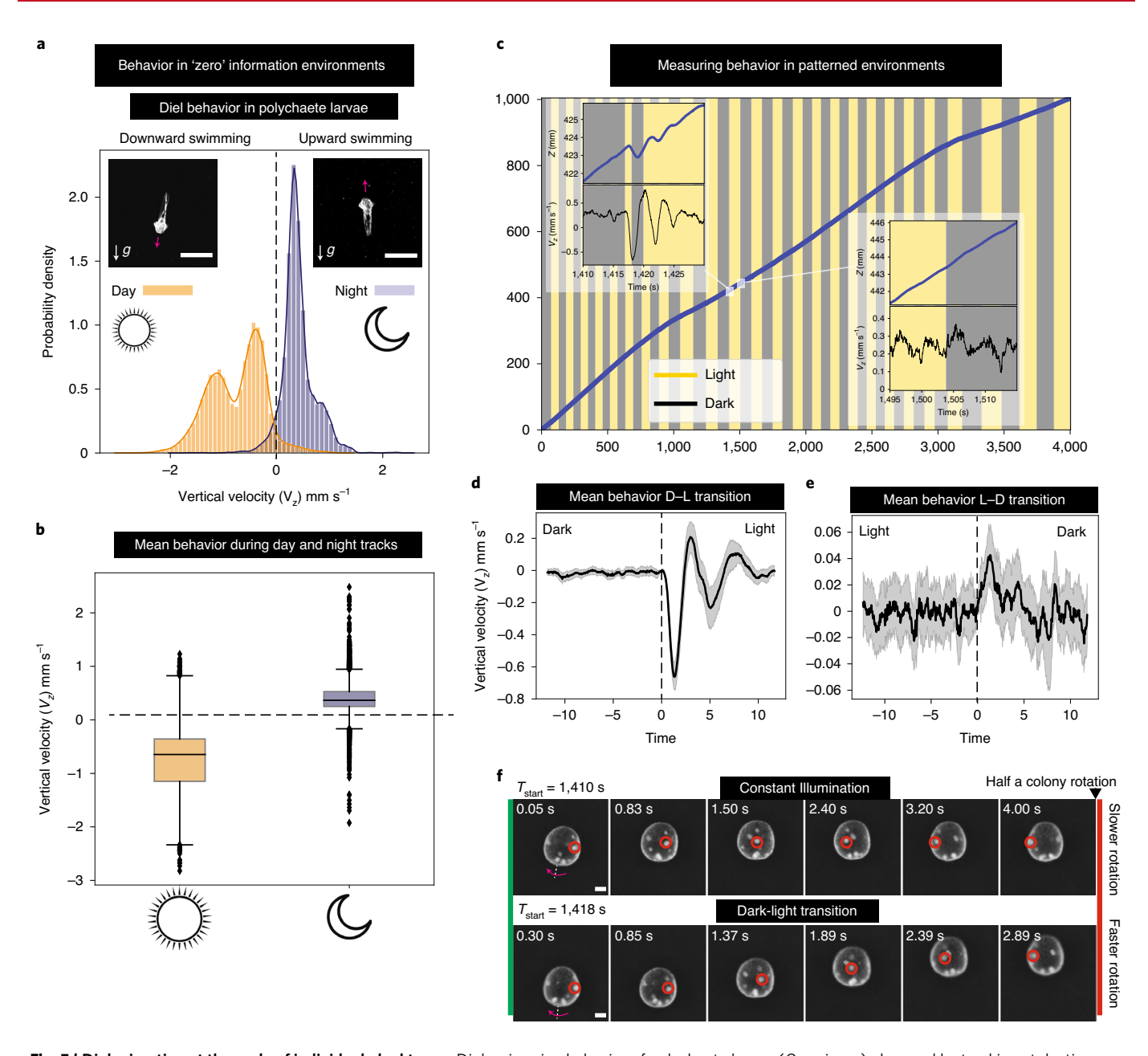


Fig. 5 | Diel migration at the scale of individual plankton. **a**, Diel swimming behavior of polychaete larvae (Owenia sp.) observed by tracking at daytime (between 13:00 and 15:00 local time) and night-time hours (between 22:00 and 00:00, local time). Vertical velocity distributions showed significant differences with swimming velocities being downward and upward, during the day and night, respectively, with all other experimental conditions maintained as constant (Supplementary Video 5) (inset, larvae images during day and night tracks; scale bar, 250 µm). **b**, Vertical velocities over several tracks of different organisms (for both **a** and **b**, n = 6 distinct organisms during daytime with total track duration 360 s and n = 5 distinct organisms during night-time with total track duration 617 s). The box represents the interquartile range, whiskers represent the range of the data and the line represents the median. **c-g**, Behavior in depth-patterned environments. Swimming behavior of the colonial alga *Volvox aureus* with ambient light conditions patterned such that a change in 'virtual depth' of 20 mm triggers a D-L or L-D transition. A track of a single *Volvox* colony swimming ≈ 1 m showing 25 transitions each of D-L and L-D. Microscale behavioral changes accompany the D-L transitions (left inset, vertical displacement and vertical velocity), whereas the swimming behavior remains unchanged during L-D transitions (right inset, Supplementary Video 6) (**c**). Behavior averaged across 25 D-L transitions by aligning vertical velocity time traces at the first D-L transition point (mean, solid black line and 95% CI, filled gray region) shows the highly repeatable nature of these transitions (**d**). In contrast, the behavior at a L-D transition is relatively unaffected (**e**). Under constant illumination (light or dark), *V. aureus* colonies rotate about their swimming direction at a constant rate of about 0.125 \pm 0.014 s⁻¹ (measured over n = 18 randomly chosen time windows, each of duration -3 s), as me

While the measured trajectories can be used to estimate long-term rates of dispersal in plankton, they also capture microscale behavior repertoires and in general, contain a wealth of information at multiple scales. To characterize the complexity of plankton behaviors

at different scales, we made use of an information-theoretic metric, namely multiscale entropy analysis⁴⁴. We calculated the sample entropy (a measure of the rate of information generation in a time series) of serially coarse-grained vertical velocity time series, giving

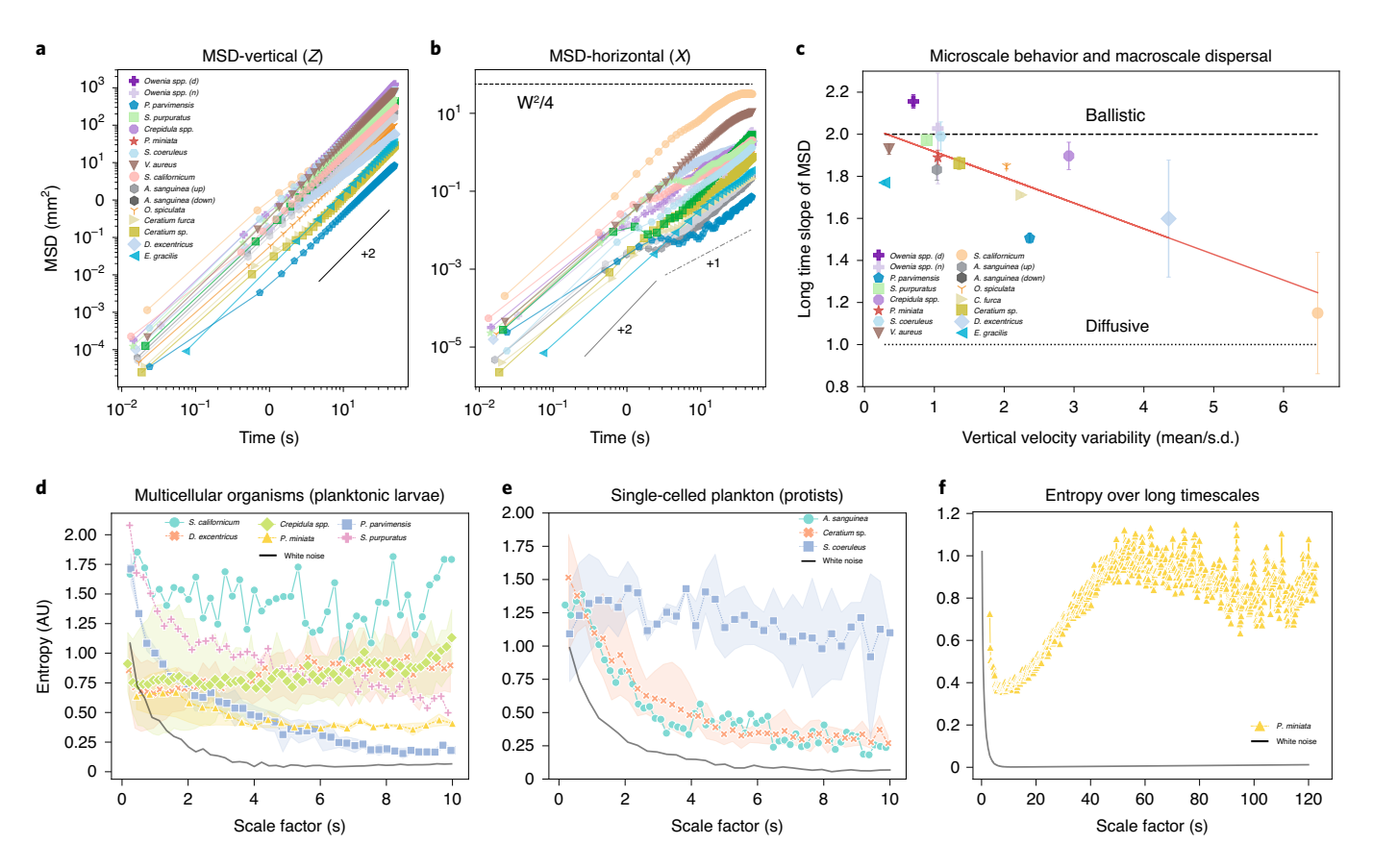


Fig. 6 | Scale-free tracking allows comparative multiscale analysis of gravity-biased behaviors across plankton species. a,b, MSDs across 14 plankton species spanning eight phyla, consisting of both unicellular and multicellular organisms. **c**, Microscale behaviors can be connected to macroscale dispersal rates by measuring the long time slopes of MSDs, revealing a negative correlation to variability (s.d. scaled by mean) of vertical velocity (r = -0.812 P = 0.0001). Error bars represent s.e.m. of the fit used to obtain the long time slope (Supplementary Note 1.1.3, Supplementary Table 2 and Methods detail number of organisms). **d,e**, Multiscale entropy analysis of vertical velocity time series for multicellular (**d**) and unicellular (**e**) plankton quantifies the complexities of plankton behaviors across timescales and reveals distinct behavioral signatures of plankton species (lines and symbols correspond to the mean and shaded regions to 95% CI). The solid black line corresponds to the entropy curve for Gaussian white noise with the same statistics as the trajectory with the largest s.d. in velocity. **f**, Long tracks (O(hours)), made possible by our method allow entropy to be calculated over longer coarse-graining scales, revealing peaks in information content that would be inaccessible for shorter tracks.

a measure of entropy as function of coarse-graining timescale. We find that this measure can distinguish between plankton trajectories, even in cases where the trajectories look qualitatively similar (Fig. 6d,e). Using this method, we can group plankton behaviors into two broad categories: (1) plankton that exhibit monotonically decreasing entropy with coarsening time, implying that behavioral variability occurs at the smallest timescales, as is typical of plankton which swim up or down at a steady speed and without significant behavioral changes over longer timescales; and (2) plankton that display more complex behaviors, such as the feeding events of P. miniata larvae, the repeated dives of S. californicum and the rapid ciliary reversals in Dendraster excentricus, exhibit entropy that does not decay, even at the largest timescales considered (Fig. 6d). Remarkably, among the single-celled organisms, S. coeruleus displays a nondecaying entropy curve (Fig. 6e) owing to its pattern of ciliary reversals, highlighting the commonality of behaviors across unicellular and multicellular plankton.

The entropy analysis also demonstrates the utility of collecting very long tracks. Long trajectories (O(hours)) allows us to calculate entropic measures over large coarsening timescales and still retain sufficient data points for statistical robustness. We demonstrate this for P.miniata larvae (Fig. 6f), where the entropy initially decreases but then rises again to peak at an intermediate timescale due to the 'blink' behaviors that punctuate long periods of upward

swimming (Fig. 4). The ability to track for several hours along with time-varying environmental cues, such entropic measures, allow a new means to detect subtle changes in plankton behaviors. Synthesis of our tracking methods with these new analysis tools enables a new class of behavioral assays to compare plankton across the tree of life.

Discussion

The scale-free tracking microscopy method presented here lays the foundation, in the form of a new microscope tracking stage, as well as an open and accessible tracking microscopy framework on which a wide range of optical, biochemical and physical experimental capabilities can be built. By adding modules to the optical tracking microscope such as epi-fluorescence, differential interference contrast, light sheet, phase-contrast or X-ray microscopy, we foresee measurements that directly link any planktonic cell's physiological state, such as the phase of cell cycle, to its virtual depth in the water column. In the case of small aquatic organisms whose behavior is governed by a neuronal system, we foresee that our methods will allow optical recording of individual neurons, while concurrently measuring behavior, which has been previously limited to horizontal tracking methods for other organisms^{9,12,45}. While we have developed a system geared toward measuring microscale objects, a similar approach of using a 'hydrodynamic treadmill' can be applied to study macroscale plankton. In an interesting convergence of

ideas, while preparing this manuscript we found an earlier effort where a circular chamber was used, along with manual observation and input by a human operator, to track macroscale plankton⁴⁶. In the future, such earlier efforts could be extended by including modern electronics and imaging systems to create an autonomous vertical tracking system for macroscale plankton.

In a vertically stratified ocean, plankton read multiple cues from the environment, such as light, temperature, salinity and pressure, to make behavioral decisions. The capacity to independently control these cues in the laboratory, akin to a virtual-reality setting, enables us to design experiments with contradictory or correlative environmental landscapes to estimate how organisms integrate these information sources to pattern their behaviors. While we have already demonstrated this for the case of varying light intensity as a function of depth, extending this method to include light spectrum, polarization and direction is also readily possible. In the future, we also envision patterning other environmental cues, such as chemical concentration and hydrostatic pressure, which can be achieved by maintaining fluidic access to the rotating fluidic chamber²⁰.

In our rapidly changing oceans, ecosystem models for plankton biogeography are becoming increasingly important for predicting the effects of these changes on plankton distribution^{5,47,48}, as well as on the carbon sequestration capacity of the biological pump⁴⁹. However, so far, the biological components of these models do not capture multiscale plankton behavior. This has mainly been due to a dearth of such behavioral data⁵ for different plankton species. Both our tool and results presented here take a step toward addressing this marked knowledge gap. Just as there has been a concerted effort to understand metabolic networks in plankton ecosystems at cell-biological and genomic levels⁵⁰, we foresee that scale-free tracking microscopy and related methods will allow a new class of behavioral datasets to be measured, which enable physiological and cell-biological insights into how plankton behaviors respond to key environmental parameters. Such 'behavioral ecology' of plankton is more crucial now than ever before as we seek to understand how plankton communities respond to a rapidly changing ocean. We anticipate that the tools and techniques presented here will provide a new window into the secret lives of plankton and oceanic ecosystems at the finest resolution.

Online content

Any methods, additional references, Nature Research reporting summaries, source data, extended data, supplementary information, acknowledgements, peer review information; details of author contributions and competing interests; and statements of data and code availability are available at https://doi.org/10.1038/s41592-020-0924-7.

Received: 6 March 2020; Accepted: 14 July 2020; Published online: 17 August 2020

References

- 1. Bar-On, Y. M., Phillips, R. & Milo, R. The biomass distribution on Earth. Proc. Natl Acad. Sci. USA 115, 6506–6511 (2018).
- Field, C. B., Behrenfeld, M. J., Randerson, J. T. & Falkowski, P. Primary production of the biosphere: integrating terrestrial and oceanic components. *Science* 281, 237–240 (1998).
- Menden-Deuer, S. & Kiørboe, T. HORIZONS small bugs with a big impact: linking plankton ecology with ecosystem processes. J. Plankton Res. 38, 1036–1043 (2016).
- Azam, F. Microbial control of oceanic carbon flux: the plot thickens. Science 280, 694–696 (1998).
- McManus, M. A. & Woodson, C. B. Plankton distribution and ocean dispersal. J. Exp. Biol. 215, 1008–1016 (2012).
- Schuech, R. & Menden-Deuer, S. Going ballistic in the plankton: anisotropic swimming behavior of marine protists. *Limnol. Oceanogr. Fluids Environ.* 4, 1–16 (2014).

 von Wangenheim, D. et al. Live tracking of moving samples in confocal microscopy for vertically grown roots. eLife 6, e26792 (2017).

- 8. Berg, H. C. How to track bacteria. Rev. Sci. Instrum. 42, 868-871 (1971).
- 9. Kim, D. H. et al. Pan-neuronal calcium imaging with cellular resolution in freely swimming zebrafish. *Nat. Methods* **14**, 1107–1114 (2017).
- Darnige, T. et al. Lagrangian 3D tracking of fluorescent microscopic objects in motion. Rev. Sci. Instrum. 88, 055106 (2017).
- Drescher, K., Goldstein, R. E., Michel, N., Polin, M. & Tuval, I. Direct measurement of the flow field around swimming microorganisms. *Phys. Rev. Lett.* 105, 1–4 (2010).
- Cong, L. et al. Rapid whole-brain imaging of neural activity in freely behaving larval zebrafish (*Danio rerio*). eLife 6, 1–20 (2017).
- Ploug, H. & Jørgensen, B. B. A net-jet flow system for mass transfer and micro electrode studies in sinking aggregates. *Mar. Ecol. Prog. Ser.* 176, 279 (1999).
- Drescher, K., Leptos, K. C. & Goldstein, R. E. How to track protists in three dimensions. Rev. Sci. Instrum. 80, 1–7 (2009).
- Verasztó, C. et al. Ciliary and rhabdomeric photoreceptor-cell circuits form a spectral depth gauge in marine zooplankton. eLife 7, 1–19 (2018).
- Sauma-Pérez, T., Johnson, C. G., Yang, L. & Mullin, T. An experimental study of the motion of a light sphere in a rotating viscous fluid. *J. Fluid Mech.* 847, 119–133 (2018).
- Van Nierop, E. A. et al. Drag and lift forces on bubbles in a rotating flow. J. Fluid Mech. 571, 439–454 (2007).
- Mukundakrishnan, K., Hu, H. H. & Ayyaswamy, P. S. The dynamics of two spherical particles in a confined rotating flow: Pedalling motion. *J. Fluid Mech.* 599, 169–204 (2008).
- 19. Wolf, A. & Schwarz, R. P. Culture Vessel. NASA technical paper 3143 (1999).
- Schwarz, R. P., Goodwin, T. J. & Wolf, D. A. Cell culture for three-dimensional modeling in rotating-wall vessels: an application of simulated microgravity. J. Tissue Cult. Methods 14, 51–57 (1992).
- Salzen, E. A. The density of sea urchin eggs, embryos and larvae. Exp. Cell Res. 12, 615–625 (1957).
- Leal, L. G. Advanced Transport Phenomena: Fluid Mechanics and Convective Transport Processes, Vol. 7 (Cambridge University Press, 2007).
- Marcos, F. H. C., Powers, T. R. & Stocker, R. Bacterial rheotaxis. *Proc. Natl Acad. Sci. USA* 109, 4780–4785 (2012).
- Rusconi, R., Guasto, J. S. & Stocker, R. Bacterial transport suppressed by fluid shear. Nat. Phys. 10, 212–217 (2014).
- Mathijssen, A. J. T. M. et al. Oscillatory surface rheotaxis of swimming E. coli bacteria. Nat. Commun. 10, 7–9 (2019).
- Strathmann, R. R. Larval feeding in echinoderms. *Integr. Comp. Biol.* 15, 717–730 (1975).
- Strathmann, R. R. & Grünbaum, D. Good eaters, poor swimmers: compromises in larval form. *Integr. Comp. Biol.* 46, 312–322 (2006).
- Emlet, R. B. Flow fields around ciliated larvae: effects of natural and artificial tethers. Mar. Ecol. Prog. Ser. 63, 211–225 (1990).
- Gonzalez, P., Jiang, J. Z. & Lowe, C. J. The development and metamorphosis
 of the indirect developing acorn worm *Schizocardium californicum*(Enteropneusta: Spengelidae). Front. Zool. 15, 1–24 (2018).
- 30. Keeling, P. J. & del Campo, J. Marine protists are not just big bacteria. *Curr. Biol.* 27, R541–R549 (2017).
- Cheriton, O. M., McManus, M. A., Stacey, M. T. & Steinbuck, J. V. Physical and biological controls on the maintenance and dissipation of a thin phytoplankton layer. *Mar. Ecol. Prog. Ser.* 378, 55–69 (2009).
- Zimorski, V., Rauch, C., Van, J. J., Tielens, A. G. M. & Martin, W. F. (eds.) Euglena: Biochemistry, Cell and Molecular Biology. 979 (2017).
- Kim, I.-H., Prusti, R. K., Song, P.-S., Häder, D.-P. & Häder, M. Phototaxis and photophobic responses in *Stentor coeruleus* action spectrum and role of Ca2⁺ fluxes. *Biochim. Biophys. Acta* 799, 298–304 (1984).
- Mackie, G. O., Spencer, A. N. & Strathmann, R. Electrical activity associated with ciliary reversal in an echinoderm larva. *Nature* 223, 1384 (1969).
- Gemmell, B. J., Jiang, H. & Buskey, E. J. A new approach to micro-scale particle image velocimetry (μPIV) for quantifying flows around free-swimming zooplankton. J. Plankton Res. 36, 1396–1401 (2014).
- Nielsen, L. T. & Kiørboe, T. Feeding currents facilitate a mixotrophic way of life. ISME J. 9, 2117–2127 (2015).
- Conzelmann, M. et al. Neuropeptides regulate swimming depth of *Platynereis* larvae. *Proc. Natl Acad. Sci. USA* 108, E1174–E1183 (2011).
- 38. Fenchel, T. & Ockelmann, K. W. Larva on a string. *Ophelia* **56**, 171–178
- Gilpin, W., Prakash, V. N. & Prakash, M. Vortex arrays and ciliary tangles underlie the feeding-swimming trade-off in starfish larvae. *Nat. Phys.* 13, 380–386 (2017).
- Pernet, B. in Evolutionary Ecology of Marine Invertebrate Larvae, Vol. 1 (Oxford University Press, 2018).
- Jékely, G. et al. Mechanism of phototaxis in marine zooplankton. Nature 456, 395–399 (2008).

- 42. Tosches, M. A., Bucher, D., Vopalensky, P. & Arendt, D. Melatonin signaling controls circadian swimming behavior in marine zooplankton. *Cell* **159**, 46–57 (2014).
- 43. Drescher, K., Goldstein, R. E. & Tuval, I. Fidelity of adaptive phototaxis. *Proc. Natl Acad. Sci. USA* 107, 11171–11176 (2010).
- Costa, M., Goldberger, A. L. & Peng, C. K. Multiscale entropy analysis of biological signals. *Phys. Rev. E* 71, 1–18 (2005).
- Nguyen, J. P. et al. Whole-brain calcium imaging with cellular resolution in freely behaving C. elegans. Proc. Natl Acad. Sci. USA 113, E1074-81 (2016).
- Hardy, A. C. & Bainbridge, R. Experimental observations on the vertical migrations of plankton animals. J. Mar. Biol. Assoc. UK 33, 409–448 (1954).
- 47. Cowen, R. K. & Sponaugle, S. Larval dispersal and marine population connectivity. *Annu. Rev. Mar. Sci.* 1, 443–466 (2008).
- 48. Cowen, R. K., Lwiza, K. M. M., Sponaugle, S., Paris, C. B. & Olson, D. B. Connectivity of marine populations: open or closed? *Science* **287**, 857–859 (2000).
- 49. Boyd, P. W., Claustre, H., Levy, M., Siegel, D. A. & Weber, T. Multi-faceted particle pumps drive carbon sequestration in the ocean. *Nature* **568**, 327–335 (2019).
- DeLong, E. F. The microbial ocean from genomes to biomes. Nature 459, 200–206 (2009).

Publisher's note Springer Nature remains neutral with regard to jurisdictional claims in published maps and institutional affiliations.

© The Author(s), under exclusive licence to Springer Nature America, Inc. 2020

Methods

Circular fluidic chamber construction. The circular fluidic chamber was custom-fabricated from four parts: two spacer rings machined out of aluminum, which were sandwiched between clear, scratch-resistant acrylic sheets, resulting in an annular volume that was optically accessible from both sides (Supplementary Fig. 1). Alternatively, the acrylic sheets can be replaced by 1.1-mm thick Borofloat glass (Precision Glass and Optics) and the spacer by CNC machined aluminum rings (Supplementary Fig. 1d,e), with O-rings used to achieve a seal. The second design has the advantage of allowing the chamber to be taken apart and autoclaved. The dimensions of the resulting annular volume were given by R_i , R_o and W. Typical values of these parameters used in our experiments were $R_i = 85 \, \text{mm}$, $R_0 = 100-115$ mm and W = 3-6 mm, resulting in cross-sectional dimensions $L \times W$, where $L = R_o - R_i$. Silicone adhesive (100%; GE silicone) was used to bond the various layers of the circular fluidic chamber to provide a biocompatible seal, which is also gas permeable to allow long-term experiments. Inlet and outlet ports made via luer attachments (Cole-Parmer) allowed the chamber to be completely filled with fluid and also allowed objects of interest to be introduced.

Motorized stages for tracking. The circular fluidic chamber was attached to a fine rotational stage using a high precision shaft (Phidgets) and rotational bearings (Robotshop) via a torsional-beam coupler (Pololu Robotics) (Extended Data Fig. 1). The rotational stage consisted of a NEMA-11 stepper motor mated to a 100:1 gearbox (Phidgets), with a horizontal rotational axis (Extended Data Fig. 1). This arrangement allowed the chamber to be rotated with an angular resolution of $19\pm1\,\mu$ rad per step, resulting in a tangential linear increment of $1.73\pm0.08\,\mu$ m per step at the center line of the annulus. The rotation of the stage was measured using optical encoders (Phidgets) with a resolution of $105.2\,\mu$ rad per pulse. The rotational stage and bearings were mounted on height adjustable posts (ThorLabs) that were adjusted to provide a horizontal axis.

The two other motion axes (*x* and *y*) were implemented using standard off-the-shelf translational stages driven by stepper motors (Haijie Technology). In our first implementation, the optical assembly was attached to the *xy* stages, such that tracking in the *xy* directions was achieved by translating the optical assembly to follow the object (Extended Data Fig. 1b).

In the latest version of the microscope, all degrees of freedom were implemented on the circular fluidic chamber (Extended Data Fig. 1a). Briefly this was performed by mounting the circular fluidic chamber on a rotational stage, which was in turn mounted on an xy translational stage. The optical system in these cases is fixed in the laboratory reference frame allowing for a lot more flexibility in the design and allowing the inclusion of advanced state-of-the-art microscopy systems (Extended Data Fig. 1a).

Optical system. We constructed a light microscope focused on either the 3 O' clock or 9O' clock position of the circular fluidic chamber, such that rotational motion of the chamber resulted in approximately vertical motion (along the z direction) in the optical FOV (Extended Data Fig. 1). The optical assembly was mounted on motorized translational xy stages for motion compensation in the horizontal directions (Extended Data Fig. 1b) or alternatively fixed in the laboratory reference with all tracking implemented on the stage (Extended Data Fig. 1a). The latter is more suitable for implementing multiple optical paths and state-of-the-art microscopy modalities. The optical assembly consisted of a lens assembly with an incorporated liquid lens (Corning, Varioptic or -2 to +3 Diopter Focus Tunable lens from Optotune, 16-mm aperture), which served as the imaging objective (finite conjugate configuration), coupled to a CMOS camera (DFK 37BUX273, The Imaging Source), capable of full-resolution imaging (1,440 × 1,080 pixels) at 238 Hz, resulting in an optical FOV of 2,293 μ m \times 1,720 μ m. The imaging system was modular so that different modalities could be interchanged. For tracking we used dark-field imaging using a ring LED assembly situated on the opposite side of the fluidic chamber (Extended Data Fig. 1). We primarily used red (635 mm) LEDs (Supplementary Fig. 17) to image, as this does not induce phototactic behaviors in most organisms. Images captured on the camera sensor were processed using a custom image-processing pipeline implemented on a standard desktop computer at rates of 100 Hz.

Control system for tracking. Images for tracking were obtained from the CMOS sensor at rates of 100 Hz and processed using a custom image-processing pipeline implemented using Python on a desktop computer (Supplementary Fig. 2a). This pipeline consisted of separate organism trackers for lateral (xz) and axial (y) positions. For lateral positions, an initial region of interest containing the object was selected by the user and this object was tracked in further frames using an open source object tracking algorithm available on OpenCV-Python⁵¹ (Supplementary Fig. 3). This algorithm was robust enough to track the same object over a long time (1 d), even in the presence of other similar-looking objects, organisms and debris. As an alternative, to take advantage of computers that have a graphics processing unit, we utilized a hardware-accelerated object-tracking algorithm⁵² that allowed a combination of robust tracking and high frame rates (up to 200 Hz). In all cases, the output of the organism tracker was the lateral position ($x_{obj}z_{obj}$) of the object relative to the center of the microscope's FOV. This output was fed through a proportional-integral-derivative controller,

which in turn calculated the error signals that were sent to the motorized stages (Supplementary Fig. 2a).

Focus tracking. For estimating the axial position of objects, a separate focus-tracking algorithm was developed. This used a liquid lens (Caspian u-25H0−075, Varioptic, Corning or −2 to +3 Diopter Focus Tunable lens from Optotune, 16-mm aperture) to rapidly scan the focal plane and obtain image stacks at up to 30 volumes s⁻¹ over a depth range of 50–500 µm (Supplementary Fig. 2b,c and Supplementary Fig. 3). A focus measure of an image was estimated using the image intensity variance53,54 (Supplementary Fig. 3). A peak-finding algorithm was further used to determine the focal plane position corresponding to the best focus and hence the object's position. This estimated position was fed to a proportional controller, with a tunable gain and the resulting error signal was used to move the y axis stage to follow the object (Supplementary Fig. 2c). We characterized the tracking performance of this method by tracking a 250-µm bead mounted to a motorized stage that allowed prescribed motion of the bead along the optical axis (Supplementary Fig. 4a). This bead was then tracked using our focus-tracking strategy by obtaining volume scans with the liquid lens and translating the optical assembly to track the object (Supplementary Fig. 4b). We characterized the tracking performance as a function of the scanning amplitude of the liquid lens and the tunable gain and found an optimal range for these parameters (see Supplementary Fig. 4c).

The error signals for all three axes were sent to a motion control unit, which was an Arduino-Due microcontroller (Arduino). The microcontroller, in turn, was used to calculate motion profiles for the motorized stages. These signals were sent to a dedicated stepper motor driver for each motorized stage axis (Big Easy Driver, Sparkfun), which used the Allegro A4988 stepper driver chip. The positions of the stages were measured using rotary optical encoders (HKT22, Phidgets) with a quadrature resolution of 600 counts per revolution.

Loading of the circular fluidic chamber and ensuring thermal equilibration. Before experiments were conducted, the fluidic chamber was passivated by filling it with 5% BSA solution (Thermo Fisher Scientific) and allowing it to sit for 1 h. After this treatment, the fluidic chamber was rinsed twice with the standard solution to be used for the experiments. For the actual experiments, the chamber was completely filled with the appropriate standard solution, through the luer attachments, taking care to avoid the formation of bubbles. Once the chamber was filled, it was mounted on the rotational stage within an enclosure set at 22 °C using a temperature control unit (AirTherm SMT, World Precision Instruments). During this time, the fluid suspension containing the objects or organisms to be tracked was also stored within the enclosure. After this, a fluid mixing protocol was activated to achieve thermal equilibrium between the chamber and fluid. Such a thermal equilibration was necessary to prevent thermally driven flows from occurring in the chamber during the experiments. The mixing protocol consisted of a rotational motion of the chamber and periodically reversing the rotation direction. These motions lead to shear-enhanced mixing of fluid in the chamber and a correspondingly more effective heat transfer, both between azimuthally separated fluid parcels, as well as between the fluid and the chamber. This mixing protocol was carried out for 10 min before introducing the objects to be tracked. After this protocol, the average background fluid motion when the fluidic chamber was at rest was measured using particle image velocimetry and was found to typically be <20 µm s⁻¹ (Supplementary Fig. 5). Once thermal equilibrium was achieved, the objects or organisms to be tracked were introduced and the above equilibration procedure was again run for 10 min to evenly suspend the objects or organisms in the fluid. Once this procedure was completed, tracking could be started. This was achieved by manually locating an object of interest and then starting the automated tracker (Supplementary Video 1). Care was also taken to ensure significant air circulation in the experimental enclosure and to prevent sources of heat from being present near the fluidic chamber, as these can cause thermally driven flows to occur during long-term imaging.

Abiotic experiments. For validating our experiments, we used density marker beads of known size and density purchased from Cospheric (Supplementary Table 3). These beads have a precisely calibrated density that is slightly higher than water, as well as a mono-disperse size range (Supplementary Table 3). We measured the sedimentation velocity of the beads as a means to validate our tracking method and microscope. To perform this calibration, beads were tracked in two ways. As a control, Eulerian tracks of beads were obtained by allowing them to sediment down a vertical cuvette with a height of 150 mm and cross-sectional dimensions $15\,\mathrm{mm}\times3\,\mathrm{mm}$. The beads were imaged as they sedimented past a fixed camera mounted to image in the vertical plane at a location at the middle of the cuvette (Supplementary Fig. 6b), so as to avoid end effects. Lagrangian tracks of the density marker beads were obtained by tracking them using the circular fluidic chamber and tracking methodology developed in this work (Supplementary Fig. 6a). Each bead was tracked for 1 min, after which the track was stopped and a new bead was tracked. The sedimenting velocity, for both the tracking methods above, was obtained by a linear fit of measured time traces of vertical displacement. The measured sedimentation velocities (n=10 tracks per bead per method) are shown in Supplementary Fig. 6c and were found to be in close agreement.

Marine invertebrate larvae experiments. The larvae used for experiments were obtained by fertilizing adult animals collected off the coast of Monterey, CA, USA. The culturing procedure for larvae matched standard protocols in the field. Before experiments, the larvae were transferred to filtered sea water and allowed to acclimatize for 1 h. Larvae were transferred to the circular fluidic chamber using tubing at least three-times their body size using gentle suction.

Environmental patterning experiments with Volvox. Volvox aureus colonies were obtained from Carolina Inc. and cultured in Volvox medium (UTEX). For the environmental patterning experiments, we used a white LED array (Adafruit) (Extended Data Fig. 1a and Supplementary Fig. 17) mounted at the ceiling of our experimental enclosure, which provided a uniform top illumination at the sample location at the 3 o'clock position of the circular fluidic chamber. The intensity of the LEDs was controlled using a pulse-width-modulation signal from the Arduino microcontroller, in turn controlled by the desktop computer based on the virtual depth of the tracked organism (Supplementary Fig. 2a). Using this system any temporal (and hence 'virtual-depth'-based) intensity profile could be programmed into our experiments as a function of the virtual depth of the organism being tracked. In our experiments we simulated an artificial profile that alternated between light and dark for every 20 mm in height gained by the organism. Red (625 mm) LEDs (Supplementary Fig. 17) were used to image the organisms, as this is a wavelength to which Volvox is insensitive.

Single-cell tracking experiments. A. sanguinea and Ceratium sp. dinoflagellates were isolated from plankton tows conducted off the pier of the Monterey marina, Monterey, CA. E. gracilis and S. coeruleus cultures were obtained from Carolina Biological Supply and imaged after a few days' acclimatization at room temperature (22 °C). Latex beads of 1 µm in diameter were included for particle image velocimetry measurements.

Statistics. To compare velocity distributions between different conditions, the Kolmogorov–Smirnov two-sample nonparametric test was used. This test reports the distance between two distributions and associated P values. These statistical metrics are included alongside the corresponding results in the main text and figure legends. Significant differences were reported based on the calculated distance between the distributions and associated P values. For all experiments involving marine larvae, the number of distinct organisms used are reported alongside the results and also summarized in Supplementary Table 2. For single cells, the following number of distinct organisms were tracked: A. sanguinea, n = 7 organisms; Ceratium sp., n = 5; E. gracilis, n = 7 and S. coeruleus, n = 5.

Reporting Summary. Further information on research design is available in the Nature Research Reporting Summary linked to this article.

Data availability

The datasets generated during and/or analyzed during the current study are available in the manuscript or the Supplementary Information and are available from the corresponding author upon request.

Code availability

Data collection was performed using the tracking microscope described in the study. The microscope used custom firmware for controlling the stages written in C++ using open source Arduino libraries and custom subroutines. The software for GUI interactions and on-the-fly image analysis was written using the PyQt API in Python 3.6, using both open source libraries and custom subroutines.

Both firmware and software codebases have been hosted at the following public repositories: https://github.com/deepakkrishnamurthy/gravitymachine-research and https://github.com/deepakkrishnamurthy/gravitymachine-analysis-gui.

References

- Lukežič, A. et al. Discriminative correlation filter tracker with channel and spatial reliability. *Int. J. Computer Vis.* 126, 671–688 (2018).
- Zhu, Z. et al. Distractor-aware siamese networks for visual object tracking. Lect. Notes Comput. Sci. 11213, 103–119 (2018).
- Batten, C. F., Holburn, D. M., Breton, B. C. & Caldwell, N. H. M. Sharpness search algorithms for automatic focusing in the scanning electron microscope. *Scanning* 23, 112–113 (2001).
- Batten, C. F. Autofocusing and Astigmatism Correction in the Scanning Electron Microscope. MPhil thesis, University of Cambridge (2000).
- Strathmann, M. F. Reproduction and Development of Marine Invertebrates of the Northern Pacific Coast: Data and Methods for the Study of Eggs, Embryos and Larvae (University of Washington Press, 2017).

Acknowledgements

We thank C. Lowe and P. Bump for providing access to marine larvae and Hopkins Marine Station for access to laboratory space. We also thank the Puerto Rico Science Trust and Isla Magueyes Marine station for laboratory access. We thank E. Korkmazhan for technical assistance for an early version of the experiment. We thank R. Konte for making the drawings of marine larvae and organisms. We thank the Prakash laboratory members for fruitful discussions. D.K. was funded by a Bio-X Bowes Fellowship, H.L. was funded by a Bio-X SIGF Fellowship. A.G.L. was funded by a Simons Postdoctoral Fellowship in Marine Microbial Ecology. M.P. acknowledges support from NSF Career Award, Moore Foundation, HHMI Faculty Fellows program, NSF CCC (DBI-1548297) program and CZ BioHub Investigators program.

Author contributions

D.K. and M.P. designed the research. D.K., H.L., F.B., A.G.L., E.L. and M.P. designed the instrument. D.K., H.L., F.B., P.C., E.L. and A.G.L. built the setup. D.K., H.L., F.B., P.C., A.G.L. and M.P. performed experiments. D.K. and F.B. performed numerical simulations. D.K. performed analytical calculations. D.K., H.L. and F.B. wrote the control software. D.K., A.G.L. and M.P. analyzed the data. D.K., H.L., A.G.L. and M.P. wrote the manuscript.

Competing interests

Portions of the technology described here are part of a US patent pending (US20190000044A1) to D.K and M.P.

Additional information

Extended data is available for this paper at https://doi.org/10.1038/s41592-020-0924-7.

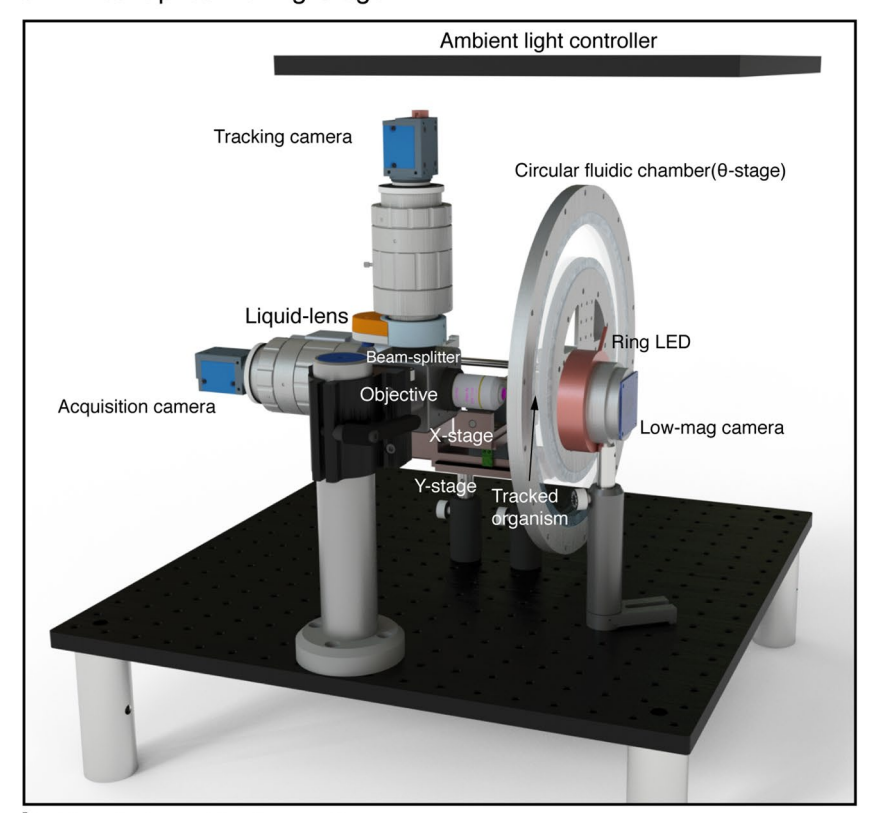
Supplementary information is available for this paper at https://doi.org/10.1038/s41592-020-0924-7.

Correspondence and requests for materials should be addressed to M.P.

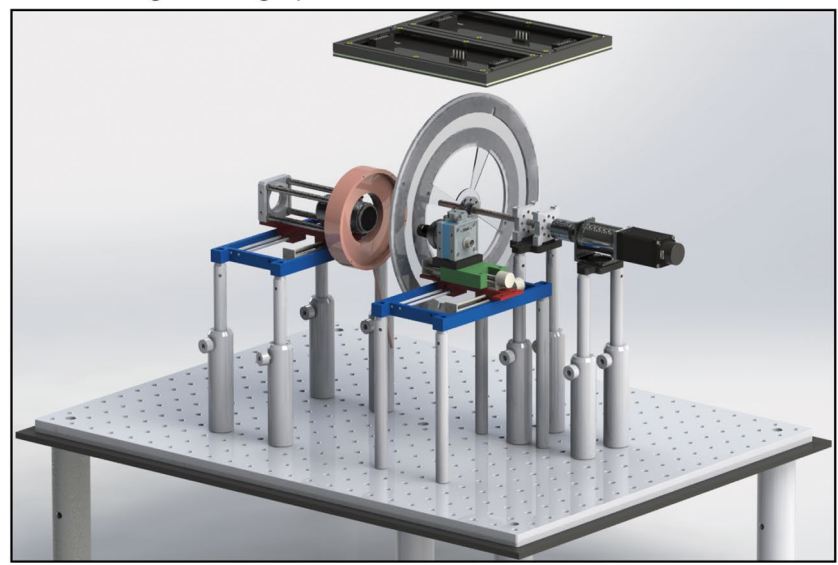
Peer review information Rita Strack was the primary editor on this article and managed its editorial process and peer review in collaboration with the rest of the editorial team.

Reprints and permissions information is available at www.nature.com/reprints.

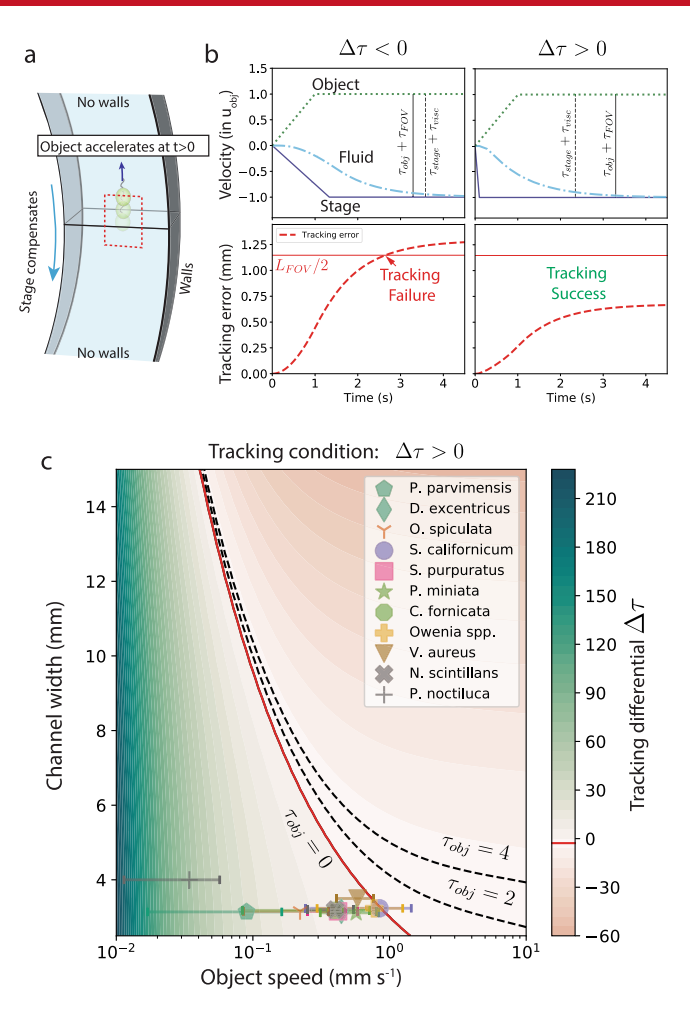
a Fixed-Optics Moving-Stage



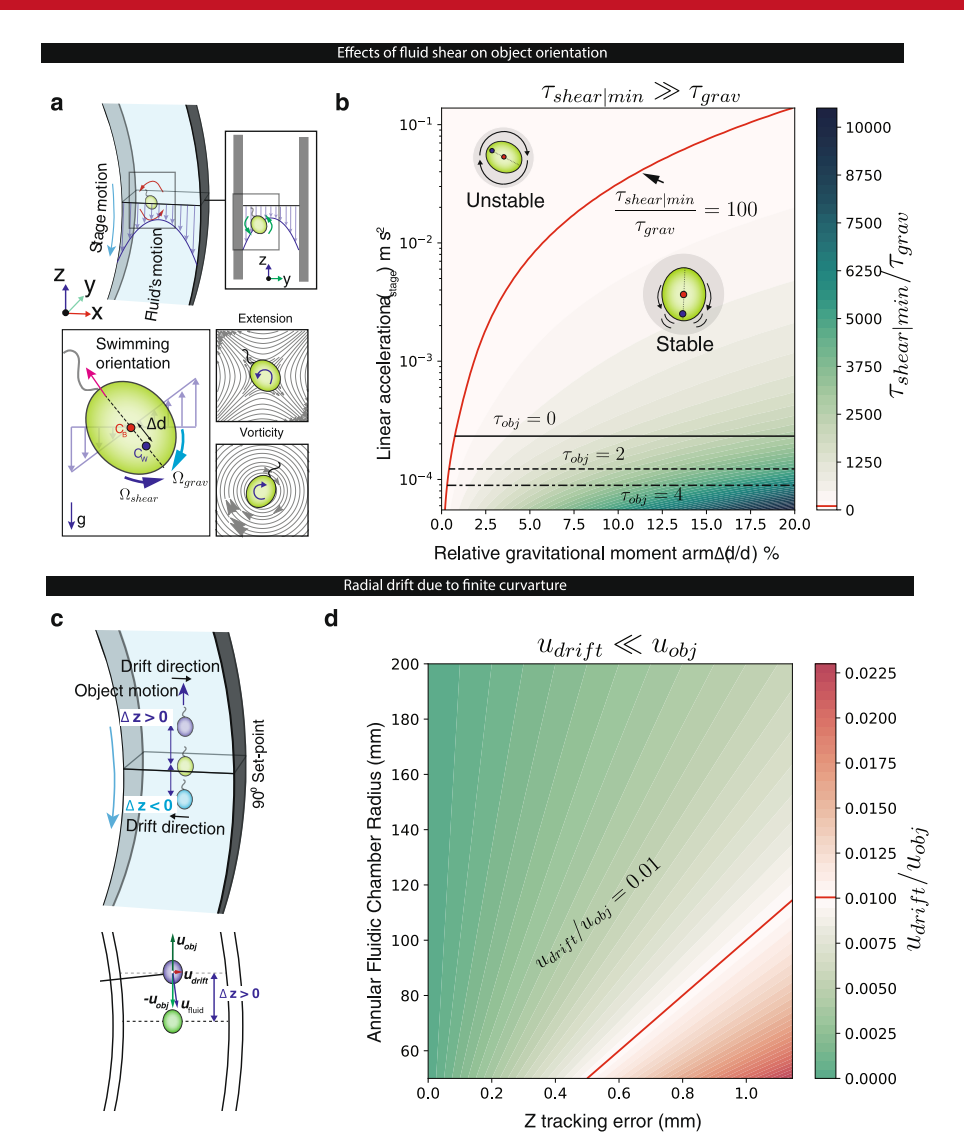
b Fixed-stage Moving-optics



Extended Data Fig. 1 | CAD rendering of the scale-free vertical tracking microscope. a, Fixed optics, moving stage configuration. This configuration gives flexibility in terms of designing the optics for the microscope and allows the addition of multiple cameras and optical paths. **b,** CAD rendering of the earlier design with fixed-stage and moving optics. This is more suitable for simple microscopy setups with a single camera.



Extended Data Fig. 2 | Design space for scale-free vertical tracking using a "hydrodynamic treadmill": Effect of stage and fluid dynamics. a, When an object accelerates vertically to achieve a maximum velocity u_{obj} over a behavioral timescale τ_{obj} , its motion is compensated by the stage. **b**, Left, velocity time traces of the object (green dotted line), stage (blue solid line) and fluid (cyan dash-dotted line), showing the viscous delay (τ_{visc}) between stage and fluid movements. Tracking success can be quantified by the difference ($\Delta \tau$) between two sets of time-scales, one related to the object ($\tau_{obj} + \tau_{FOV}$) and the other related to the stage plus fluid system ($\tau_{stage} + \tau_{visc}$), where $\tau_{FOV} = L_{FOV} / u_{obj}$ and L_{FOV} is the optical field-of-view (FOV) size. (**b**) Right, successful tracking is when the object's movements can be compensated so that its distance from the center of the optical FOV (red dashed line) never exceeds half the FOV size (solid red line). **c**, Plots of $\Delta \tau$ with respect to the chamber width (W) and object speed (u_{obj}) for $\tau_{obj} = 0$ (instantaneous velocity changes). The tracking limits (zero-crossing of $\Delta \tau$) are shown for different behavioral timescales τ_{obj} (solid, dashed and dot-dashed contour lines). Symbols (mean) and whiskers (standard deviation) correspond to various organisms (see Supplementary Table 1) which were successfully tracked for chamber widths of 3.2,3.5 and 4 mm.



Extended Data Fig. 3 | Design space for scale-free vertical tracking using a "hydrodynamic treadmill": Effect of transient fluid shear and chamber curvature. a, Rotational stage acceleration leads to a non-uniform velocity profile, which at the scale of the object is locally a simple shear flow. This shear flow (with shear rate \dot{r}), can be decomposed into an extensional and vortical component, both of which perturb the object's equilibrium orientation, in opposing directions. A gravitactic effect, due to a displaced center-of-mass and center-of-buoyancy, stabilizes the orientation and aligns it with gravity over a timescale τ_{grav} . A balance of these two effects is quantified by the ratio of time-scales $\tau_{shear/min}/\tau_{grav}$ where $\tau_{shear/min}$ is the inverse of the maximum possible shear rate during a chamber acceleration. **b,** Plot of $\tau_{shear/min}/\tau_{grav}$ with respect to stage acceleration and the gravitactic moment arm relative to object size. There is a broad region where the object orientation is highly stable ($\tau_{shear/min}/\tau_{grav} \gg 1$), implying that tracking has a negligible effect on orientation. The upper bound for stage acceleration is set by imposing the condition $\tau_{shear/min}/\tau_{grav} > 100$ (solid red curve), and the lower bound is set by the condition $\Delta \tau > 0$ in Extended Data Fig. 2c (cross-over contours shown for $\tau_{obj} = 0, 2, 4$). **c,** Top, tracking a linear motion using a circular chamber implies that, for a non-zero vertical tracking error (Δz), there is a radial drift induced in the object's motion. Bottom, this drift velocity is given by $u_{drift}(t)/u_{obj} = \Delta z/R(t)$, where R(t) is the radial position of the object at time t. **d,** Ratio of radial drift velocity to object's speed plotted as a function of the radius of the fluidic chamber center-line ($(R_i + R_o)/2$) and the vertical tracking error, showing the cross-over (red solid line) where the ratio exceeds 1%.

nature research

Corresponding author(s):	Manu Prakash
Last updated by author(s):	Jul 6, 2020

Reporting Summary

Nature Research wishes to improve the reproducibility of the work that we publish. This form provides structure for consistency and transparency in reporting. For further information on Nature Research policies, see our <u>Editorial Policies</u> and the <u>Editorial Policy Checklist</u>.

\sim			100	
St	`a:	tic	:†:	CS

For	all statistical analyses, confirm that the following items are present in the figure legend, table legend, main text, or Methods section.
n/a	Confirmed
	The exact sample size (n) for each experimental group/condition, given as a discrete number and unit of measurement
	A statement on whether measurements were taken from distinct samples or whether the same sample was measured repeatedly
	The statistical test(s) used AND whether they are one- or two-sided Only common tests should be described solely by name; describe more complex techniques in the Methods section.
X	A description of all covariates tested
\boxtimes	A description of any assumptions or corrections, such as tests of normality and adjustment for multiple comparisons
	A full description of the statistical parameters including central tendency (e.g. means) or other basic estimates (e.g. regression coefficient AND variation (e.g. standard deviation) or associated estimates of uncertainty (e.g. confidence intervals)
	For null hypothesis testing, the test statistic (e.g. <i>F</i> , <i>t</i> , <i>r</i>) with confidence intervals, effect sizes, degrees of freedom and <i>P</i> value noted <i>Give P values as exact values whenever suitable.</i>
\boxtimes	For Bayesian analysis, information on the choice of priors and Markov chain Monte Carlo settings
\boxtimes	For hierarchical and complex designs, identification of the appropriate level for tests and full reporting of outcomes
	Estimates of effect sizes (e.g. Cohen's <i>d</i> , Pearson's <i>r</i>), indicating how they were calculated
	Our web collection on statistics for biologists contains articles on many of the points above

Software and code

Policy information about availability of computer code

Data collection

Data collection was performed using the tracking microscope described in the study. The microscope used custom firmware for controlling the stages written in C++ using open-source Arduino (1.8.9) libraries and custom sub-routines. The software for GUI interactions and on-the-fly image analysis was written using the PyQt API in python 3.6, using both open-source libraries and custom sub-routines. Both firmware and software code-bases have been hosted at this public repository (https://github.com/deepakkrishnamurthy/gravitymachine-research).

Data analysis

All data analysis was carried out using Python (3.6), using both standard open-source libraries and custom scripts. These scripts have been hosted at this public github repository (https://github.com/deepakkrishnamurthy/gravitymachine-analysis-gui)

For manuscripts utilizing custom algorithms or software that are central to the research but not yet described in published literature, software must be made available to editors and reviewers. We strongly encourage code deposition in a community repository (e.g. GitHub). See the Nature Research guidelines for submitting code & software for further information.

Data

Policy information about availability of data

All manuscripts must include a data availability statement. This statement should provide the following information, where applicable:

- Accession codes, unique identifiers, or web links for publicly available datasets
- A list of figures that have associated raw data
- A description of any restrictions on data availability

The datasets generated during and/or analysed during the current study are available in the manuscript or the Supplementary Information and are available from the corresponding author upon request

Field-specific reporting				
Please select the one below that is the best fit for your research. If you are not sure, read the appropriate sections before making your selection.				
☑ Life sciences ☐ Behavioural & social sciences ☐ Ecological, evolutionary & environmental sciences				
For a reference copy of the document with all sections, see nature.com/documents/nr-reporting-summary-flat.pdf				
Life sciences study design				

All studies must disclose on these points even when the disclosure is negative.

Sample size

Samples sizes were not predetermined since the experiments were not hypothesis-driven. In all cases the reported measurements were the first of their kind and no:of samples were determined by the following constraints: Each individual organism was tracked for as long as feasible and at the conclusion of a track new organisms were tracked. The no:of organisms was determined by how many could be tracked within a typical 2 hour time window. This procedure was repeated if the number of tracks per organism was small (<3).

Data exclusions

No data pertinent to the results presented were excluded.

Replication

For each organism, the tracking experiments were repeated independently over many individuals. In all instances were a specific behavioral event was measured (eg. the behavioral transitions in invertebrate larvae, and the transient sinking of volvox colonies under illumination, and the diel behavior in polychaete larvae), the behavior was measured consistently across all individuals.

Randomization

Since the experiments were not hypothesis driven, the organisms were not separated into experimental groups and hence randomization was not applicable. During tracking experiments at the conclusion of each track, the microscope FOV was moved to a new random location in the circular fluidic chamber so as to decrease the likelihood of tracking the same organism more than once.

Blinding

All analysis was done using quantitative metrics and did not require blinding.

Reporting for specific materials, systems and methods

We require information from authors about some types of materials, experimental systems and methods used in many studies. Here, indicate whether each material, system or method listed is relevant to your study. If you are not sure if a list item applies to your research, read the appropriate section before selecting a response.

Materials & experimental systems		Methods	
n/a	Involved in the study	n/a	Involved in the study
\boxtimes	Antibodies	\boxtimes	ChIP-seq
\boxtimes	Eukaryotic cell lines	\boxtimes	Flow cytometry
\boxtimes	Palaeontology and archaeology	\boxtimes	MRI-based neuroimaging
	Animals and other organisms		
\boxtimes	Human research participants		
\boxtimes	Clinical data		
\boxtimes	Dual use research of concern		

Animals and other organisms

Policy information about studies involving animals; ARRIVE guidelines recommended for reporting animal research

Laboratory animals

The following marine invertebrate larvae were spawned under lab conditions: Owenia sp (Polychaete worm), Crepidula sp. (Snail), P. miniata (Bat Star), S. purpuratus (Purple Sea Urchin), S. californicum (Acorn worm), O. spiculata (Spiny Brittle Star), D. excentricus (Pacific Sand Dollar) and P. parvimensis (Warty Sea Cucumber). The age and other details of these larvae is provided in Supplementary Information of this paper.

Wild animals

No wild animals were used in this study.

Field-collected samples

Single-celled dinoflagellates were collected using net tows and identified using microscopy. These were maintained in L1 (minus Silica) medium at 22 C under 12:12 L/D cycles. The cultures were maintained in the lab at the end of the experiment.

Ethics oversight

No ethical approval was required for organisms used in this study.

Note that full information on the approval of the study protocol must also be provided in the manuscript.